In vitro reconstitution reveals membrane clustering and double-stranded RNA recruitment by the enteroviral AAA+ ATPase 2C

Kasturika Shankar[1,2,3,4], Marie N. Sorin[1,2,3,4], Oskar Skoglund[1,2,3,4], Selma Dahmane[1,2,3,4], Himanshu Sharma[1,2,3,4], Josy ter Beek[1,2,4], Louise Nenzén[1,2,3,4], Lars-Anders Carlson[1,2,3,4,*]

1. Department of Medical Biochemistry and Biophysics, Umeå University, Umeå, Sweden

2. Wallenberg Centre for Molecular Medicine, Umeå University, Umeå, Sweden

3. Laboratory for Molecular Infection Medicine Sweden (MIMS), Umeå University, Umeå, Sweden

4. Umeå Centre for Microbial Research (UCMR), Umeå University, Umeå, Sweden

*corresponding author: lars-anders.carlson@umu.se

Keywords: enterovirus, picornavirus, poliovirus, AAA+ ATPase, cryo-electron tomography, membrane, in vitro reconstitution, 2C

Abstract

Enteroviruses are a vast genus of positive-sense RNA viruses that cause diseases ranging from common cold to poliomyelitis and viral myocarditis. They encode a membrane-bound AAA+ ATPase, 2C, that has been suggested to serve several roles in virus replication, e.g. as an RNA helicase and capsid assembly factor. As an oligomeric peripheral membrane protein, the low solubility of 2C has hitherto impaired biochemical studies of the full-length protein. Here, we report a biochemical reconstitution poliovirus 2C association with membranes. We show that a conserved glycine divides the N-terminal membrane-binding domain of 2C into two amphipathic helix regions, AH1 and AH2. AH2 is the main mediator of 2C oligomerization, and is sufficient for its membrane binding. AH1 is the main mediator of a novel function of 2C: clustering of membranes. Cryo-electron tomography reveal that several 2C copies mediate this function by localizing to vesicle-vesicle interfaces. 2C-mediated clustering is partially outcompeted by nucleic acids, suggesting a way by which 2C can switch from an early role in coalescing replication organelles, and recruiting lipid droplets to them, to a later role where 2C assists RNA replication and particle assembly. 2C is sufficient to recruit RNA to membranes, with a preference for double-stranded RNA, thus being a candidate for the factor that localizes viral RNA replication to membranes. Finally, the *in vitro* reconstitution revealed that full-length 2C localized to a membrane has weak RNA chaperoning activity, dependent on having a free N terminus, but does not possess ATP-dependent helicase activity. Together, this study suggests two novel roles for 2C in membrane clustering and double-stranded RNA recruitment to membranes, and calls into question a role of 2C as an RNA helicase. The reconstitution of functional, 2C-decorated vesicles provides a platform for further experimental studies into this protein and its roles in enterovirus replication.

Introduction

The *Enterovirus* genus (family: *Picornaviridae*) are positive-sense single-stranded RNA (+ssRNA) viruses, whose ~7.5kb genome is encapsidated in a 30 nm non-enveloped, icosahedral capsid [1, 2]. There are hundreds of known human enteroviruses, responsible for diseases like poliomyelitis (poliovirus, PV), viral myocarditis (Coxsackievirus B3, CVB3), common cold (Rhinoviruses, RVs) and hand, foot and mouth disease (e.g., Coxsackievirus A16 and Enterovirus 71, EV71) [3-5]. In addition, their high mutation rate and frequent recombinations mean that novel enteroviruses emerge regularly [6-8]. PV, which causes the paralytic disease poliomyelitis, has been a major focus of enterovirus research and worldwide vaccination efforts. Since the launch of the Global Polio Eradication Initiative in 1988, the number of poliomyelitis cases have reduced significantly, but it continues to haunt a few countries as an endemic disease [9, 10]. There is limited progress in the production of vaccines against the many non-polio enteroviruses that cause frequent outbreaks in different parts of the world [11]. Development of pan-enteroviral drugs that inhibit conserved steps of the replication cycle is thus of importance not only for the last phase of polio eradication, but also for minimizing the risk associated with future enterovirus outbreaks, as well as for treating chronic enterovirus infections [12-15].

Enterovirus genome replication is a highly conserved process requiring the formation of cytoplasmic replication organelles (ROs) [16-18]. The ROs are formed from extensively modified cytoplasmic membranes which are turned into an assembly line for viral RNA and virus particles [19, 20]. RO membranes are obtained from several cellular sources. Initially, they come from the disassembly of the Golgi apparatus as well as from utilization of cellular cholesterol [21, 22]. In addition, ROs are enriched by fatty acids from lipid droplets, through RO-LD contacts mediated by the viral protein 2C [23]. At later time points, induction of macro-autophagy (henceforth: autophagy) provides another source of RO membranes in the form of double-membrane vesicles [24-26]. The direct dependence of enterovirus RNA replication on membranes is supported e.g. by electron microscopy autoradiography, showing that newly synthesized RNA co-localizes with RO membranes [27]. Further, subcellular fractions active in viral RNA synthesis contain membranes, and their activity is inhibited if the membranes are disintegrated by detergents [28, 29]. How viral RNA, viral proteins, and host factors arrange spatially on the cytoplasmic face of RO membranes is not known.

The enterovirus genome has one major open reading frame which is translated as a single major polyprotein, with some enteroviruses also having a smaller accessory open reading frame [30]. The major polyprotein is subsequently cleaved into eleven individual proteins by the viral proteases 2A and 3C (Fig. 1A). The non-structural proteins, contained in polyprotein regions P2 and P3, encode functions necessary for RO formation and genome replication (Fig. 1A). Amongst these is the protein 2C, a conserved, multifunctional ATPase of the AAA+ superfamily [31-33]. 2C is essential for both RNA replication and virion assembly, but its precise roles in these processes are unknown [34-38]. 2C has a central ATPase domain followed by a Zn finger and a C-terminal α-helix which engages a hydrophobic pocket of another 2C monomer to aid its oligomerization [39-42] (Fig. 1A). ATP hydrolysis by 2C is stimulated by its oligomerization [41, 43], and by binding to single-stranded RNA [44]. Interestingly, even though homologous proteins from other viruses are helicases, most publications report that 2C only has ATP-independent RNA chaperoning activity, and little-to-no ATP-dependent RNA helicase activity[44, 45]. However, it must be noted that biochemical studies on 2C have to date been carried out in simplified systems, using e.g. truncated 2C constructs, fusion proteins, and/or omitting the membrane platform on which 2C is located during infection.

The conserved, N-terminal membrane-binding domain (MBD) of 2C is necessary for virus replication [46]. It has been suggested to contain an amphipathic helix, and has been shown to be necessary and sufficient for membrane association when overexpressed in cells [46-48]. The MBD has further been described to mediate the hexamerization of poliovirus 2C [43], while the C-terminal α-helix appears sufficient to mediate hexamerization of 2C from some other enteroviruses [40]. Due to the

87 hydrophobic nature of the MBD, full-length 2C tends to aggregate during purification, thus prohibiting
88 its use in biochemical experiments. This problem has typically been circumvented by working with a
89 truncated 2C construct lacking the MBD [39-41], or by using high concentrations of detergents [44].
90 Alternatively, fusing the N-terminus of full-length 2C to the large, hydrophilic maltose-binding protein
91 (MBP) has also been reported to result in a soluble protein [43]. While all of these studies have
92 uncovered important aspects of 2C's function, they were not able to address the mechanisms of its
93 membrane binding, nor its function as a full-length protein on a membrane.

94 Here, we biochemically reconstituted the binding of purified, full-length poliovirus 2C to synthetic
95 vesicles. We suggest that the MBD is in fact composed of two amphipathic helix segments, AH1 and
96 AH2, interrupted by an absolutely conserved glycine residue. Both AH1 and AH2 are necessary for
97 complete hexamerization of 2C, whereas AH2 is sufficient for its membrane localization. A novel
98 function for AH1 is identified in tethering membranes together, and we show that 2C's membrane
99 tethering can be partially outcompeted by nucleic acid. We show that 2C is sufficient to recruit and
100 retain RNA to membranes, and that it has a strong preference for retaining double-stranded RNA at a
101 membrane. Together, these findings provide a biochemical basis for several roles of 2C in enterovirus
102 replication, and establishes a more realistic biochemical system as a basis for further investigations.

103

104 **Results**

105 **The oligomerization state of 2C is controlled by its N-terminal, bipartite amphipathic helix**

106 The membrane-binding domain (MBD) of 2C (Fig. 1A) consists of residues ~1-40 and is suggested to
107 be an amphipathic helix [46-48], but details of its structure are not known. We took a computational
108 approach to studying the MBD across enteroviruses. A multiple sequence alignment revealed that
109 several hydrophobic residues (W4, L5, F8, G17, W20, I25, F28, I29, W31, L32 and I36), polar
110 residues (S3, K6, K7, K24, K27, and K35) and P38 are broadly conserved between enterovirus species
111 (Fig. 1B). We next studied the amphipathic nature of the 1-40 region by calculating its hydrophobic
112 moment (μH) in a sliding window of 18 residues. A high value for hydrophobic moment means that a
113 helix is amphipathic (i.e. that one side is more hydrophobic than the other). The calculation suggested
114 that the MBD may, in fact, consist of two separate amphipathic helices, with the space between the
115 amphipathic regions coinciding with the conserved residue G17 (Fig. 1C). The amphipathic nature of
116 these two regions was corroborated by a helical wheel plot (Fig.S1A). Since glycine is a helix breaker
117 residue, we hypothesized that G17 in fact divides the MBD into two amphipathic helices, AH1 and
118 AH2. AlphaFold2 [49] structure predictions of 2C(1-40) of several enteroviruses indeed suggested that
119 a kink at G17 is a conserved structural feature (Fig. 1D). In addition, the structure predictions indicate
120 that AH1 has a hydrophobic surface which is offset from AH2 [50] (Fig. S1B). Together, these data
121 suggest that the MBD of 2C consists of two amphipathic helices, AH1 and AH2, and we thus set out
122 to study their individual roles in the protein.

123 Recombinant full-length 2C has been reported to be insoluble in the absence of detergents unless its
124 N-terminus is fused to a solubility-enhancing tag [39, 44]. We thus purified the N-terminally
125 His_6MBP-tagged, full-length poliovirus 2C protein (residues 1-329) and its N-terminally truncated
126 variants 2C(ΔAH1) (residues 12-329), 2C(ΔMBD) (residues 41-329) and 2C(Δ115) (residues 116-
127 329) (Fig. 2A, B, Fig. S2). The two first constructs correspond to the truncation of AH1, and AH1-2,
128 respectively, whereas the third construct corresponds to a soluble fragment which has previously been
129 crystallized [39]. Full-length 2C is a hexamer [39, 41, 43, 51]. We wanted to study the individual
130 roles of the AH1 and AH2 regions in hexamer assembly. Notably, every N-terminal truncation led to a
131 gradual shift towards higher elution volumes in size exclusion chromatography (Fig. 2B), indicating
132 that every part of the MBD plays a role in 2C oligomerization. To further dissect the role of AH1 and
133 AH2, we determined the molecular mass distribution of full-length and truncated 2C constructs. Mass

134 photometry of MBP-2C and MBP-2C(ΔAH1) at 100 nM revealed presence of monomeric protein, but
135 also high-mass peaks (Fig. 2C,D). For the full-length protein, the high-mass peak closely corresponds
136 to a hexamer, whereas the 2C(ΔAH1) high-mass peak corresponds to a pentamer, or e.g. a mix of
137 hexamer and a smaller species. The shorter constructs 2C(41-329) and 2C(116-329) were stable in
138 solution even after removal of the MBP tag, and their masses were analyzed at 38 µM and 134 µM,
139 respectively, by size exclusion chromatography coupled to multi-angle light scattering (SEC-MALS).
140 The mass estimates throughout the predominant peak for two consecutive runs were 43 kDa and 52
141 kDa for 2C(41-329), i.e. a mass intermediate between monomer (at 32.8 kDa) and dimer (Fig. 2E),
142 possibly due to an equilibrium between the two states. The predominant peak for two SEC-MALS
143 runs for 2C(116-329) gave an estimated mass of 27 kDa and 22 kDa, consistent with the expected 23.8
144 kDa of a monomer (Fig. 2F). The MBP-fused versions of these constructs both had SEC-MALS mass
145 estimates corresponding to monomers (Fig. S3A-B).

146 Taken together, the conserved glycine 17 divides the MBD into two amphipathic helices, AH1 and
147 AH2, with offset hydrophobic faces. Both AH1 and AH2 are important for hexamerization of 2C in
148 solution, and the deletion of the entire MBD only leaves 2C with a weak propensity for dimerization.

149

150 **The AH2 region mediates charge-independent binding of 2C to membranes**

151 We next wanted to study the individual roles of AH1 and AH2 in 2C's membrane binding. To this
152 end, we reconstituted the process *in vitro* using synthetic liposomes, and the purified 2C constructs
153 described above. We devised an assay in which MBP-fused 2C is first mixed with small or large
154 unilamellar vesicles (SUVs and LUVs, respectively), after which TEV protease is added to cleave off
155 the MBP tag and allow 2C to bind the liposomes (Fig. 3A). The 2C-decorated liposomes are then
156 subjected to a flotation assay, in which the liposome-containing upper fraction and liposome-free
157 lower fraction are separated. 2C and liposomes are labelled with different fluorophores (ATTO488
158 maleimide conjugated to cysteines, and ATTO647N conjugated to DOPE, respectively), allowing
159 quantification of 2C and lipids in the fractions (Fig. 3A). The lipid fluorescence readings in the upper
160 fraction were consistent across all experiments, allowing for quantitative comparisons of the amount
161 of protein bound to liposomes (Fig. S4). We first used SUVs composed of net uncharged lipids: 75
162 mol% 1-palmitoyl-2-oleoyl-glycero-3-phosphocholine (POPC), 25 mol% 1-palmitoyl-2-oleoyl-sn-
163 glycero-3-phosphoethanolamine (POPE). The SUVs had an average size of ~30 nm as determined by
164 dynamic light scattering (DLS) (Fig. S5). The addition of MBP-2C and TEV to the SUVs led to the
165 formation of two distinct SUV bands in the upper fraction (Fig. 3B, Fig. S6A). 88±11% of full-length
166 2C were found in the upper fraction, with most protein in the uppermost of the two bands (Fig. S6B).
167 MBP-fused 2C was able to associate with SUVs to a similar degree as cleaved 2C, indicating that the
168 MBD is exposed, also in the MBP fusion protein. However, later experiments would show that
169 removal of the MBP tag was necessary for functional association of 2C with membranes. Upon
170 deletion of AH1, 81±16 % of 2C(ΔAH1) was still found in the upper fraction, whereas deletion of the
171 entire MBD (AH1-AH2) led to only 10±7.4 % of 2C(41-329) being found in the upper fraction (Fig.
172 3C). Thus, the AH2 region is the main mediator of 2C membrane association.

173 We then wished to study if 2C has a preference for a given membrane charge or curvature. In side-by-
174 side flotation experiments, we quantitated 2C binding to the POPC/POPE (net uncharged) SUVs
175 described above, and SUVs consisting of 50 mol% phosphatidyl serine (POPS, net charge -1). Full-
176 length 2C and 2C(ΔAH1) showed no preference for the negatively charged POPS, whereas the binding
177 of 2C(41-329) increased from 10±7.4 % to 38±7% when POPS was included in the SUVs (Fig. 3D).
178 To determine if 2C has a membrane curvature preference, we compared 2C binding to the sonicated
179 POPC/POPE SUVs, with an average size of ~50 nm, and larger (and hence lower-curvature) LUVs
180 with the same lipid composition and an average diameter of ~2500 nm. Full-length 2C and 2C(ΔAH1)
181 showed a slight decrease in the binding to the lower-curvature LUVs (Fig. 3E), but this decrease was

182 no longer significant after normalizing for the amount of lipid present in the top fraction (Fig. S4F).In
183 summary, these data show that the AH2 region mediates strong 2C membrane binding, which is
184 neither dependent on high membrane curvature nor on negatively charged lipids.

185

186 **2C mediates lipid clustering, which is enhanced by the AH1 region**

187 In virus-infected cells, 2C is present at contact sites of ROs and lipid droplets[23], and we suspected
188 that the high-density band of 2C-coated SUVs in our flotation experiments may be an *in vitro*
189 recapitulation of 2C-mediated lipid tethering (Fig. 3B, Fig. S6B). We used DLS to investigate lipid
190 clustering by 2C. As described above, the MBP tag was cleaved from 2C in the presence of SUVs.
191 After a 30 min incubation, the size distribution of the sample was measured using DLS. The sonicated
192 SUVs were around 40 nm in size, whereas the addition of TEV protease and 0.8 μM MBP-2C to these
193 SUVs led to the formation of vesicle clusters with an average diameter of ~1 μm (Fig. 4A). 2C(ΔAH1)
194 also clustered SUVs (Fig. 4A). Defining a liposome cluster as a particle with a diameter of >100 nm(
195 2.5 times the average SUV size), we compared the percentage of clusters in reactions containing
196 different concentrations of 2C and 2C(ΔAH1). Already at 0.8 μM protein – the concentration used for
197 the flotation assays – full-length 2C generated significantly more clusters than 2C(ΔAH1) (11.5±4.0%
198 and 4.6±1.7%, respectively, Fig. 4B). At 3 μM 2C, the difference was even more pronounced, with
199 47.0±13% of liposomes being present in clusters with 2C and 12±13% for 2C(ΔAH1) (Fig. 4B). To
200 characterize the 2C-mediated vesicle clusters at nanometer resolution, we then performed cryo-
201 electron tomography (cryo-ET) on the 3 μM reaction with full-length 2C. This allowed direct
202 visualization of how 2C tethers liposomes together to form larger clusters (Fig. 4C). Typically,
203 multiple 2C densities were present on the imaged SUVs, and they were mostly found at the interface
204 between SUVs (Fig. 4C). Taken together, 2C clusters liposomes *in vitro*, and the AH1 region is
205 necessary for effective clustering.

206 **Nucleic acid binding competes with 2C membrane clustering, and 2C preferentially recruits**
207 **double-stranded RNA to membranes**

208 The enterovirus genome is replicated on the cytoplasmic face of the RO membrane [19, 52]. Since 2C
209 is a AAA+ protein and a putative RNA helicase [33, 36, 42, 44, 45, 53-56], we wondered whether 2C
210 is sufficient to recruit and retain RNA at the membrane, and whether nucleic acid binding may affect
211 2C's lipid clustering activity. To address the second question, we repeated the lipid clustering
212 experiment using full-length 2C, in the presence of increasing concentrations of nucleic acid. It was
213 previously reported that both DNA and RNA bind at the same site on 2C, and that initial binding is
214 dependent on the phosphodiester backbone [44]. Hence, we used single-stranded DNA (ssDNA)
215 oligonucleotide and measured the amount of clustering using DLS (Fig. 5A). Upon increasing the
216 concentration of ssDNA there was a consistent decrease in the percentage of clustered lipids, albeit
217 only statistically significant at 100 μM ssDNA concentration (Fig. 5B). This indicates that nucleic acid
218 binding partially outcompetes the membrane tethering activity of 2C. To directly test the hypothesis
219 that 2C recruits RNA to the membrane, and to investigate if it possesses any selectivity, we devised an
220 alternative SUV flotation assay. In this assay, 2C was no longer fluorophore-labelled. Instead, a
221 fluorophore-labeled RNA (single-stranded or double-stranded) was added in the first step of the
222 flotation assay, allowing quantitation of the amount of RNA co-migrating with the SUVs (Fig. 5C,
223 Fig. S7). 2C was able to recruit both ssRNA and dsRNA to SUVs and retain it at the membrane
224 throughout the ultracentrifugation of the flotation experiment (Fig. 5D). At identical starting
225 concentrations, dsRNA was recruited significantly more than ssRNA (Fig. 5D). The recruitment was
226 strictly dependent on 2C having a free MDB since omission of TEV protease completely abrogated the
227 RNA recruitment (Fig. 5D). Taken together, 2C recruits and retains nucleic acid to membranes, with a
228 preference for dsRNA over ssRNA, and nucleic acid binding reduces 2C-mediated membrane
229 clustering.

230

231 **Membrane-bound, full-length 2C is an ATPase and an ATP-independent RNA chaperone**

232 Several studies have sought to determine whether 2C is an active RNA helicase, but they were
233 generally conducted with protein that was truncated and/or not membrane-associated. Having
234 reconstituted the binding of full-length 2C to membranes, and shown that it recruits RNA to
235 membranes, we set out to use this more realistic system to revisit the question of 2C's helicase
236 activity. We conducted an RNA helicase assay using 2C and 2C(41-329) in the presence of SUVs. The
237 MBP-fused proteins were incubated with a dsRNA with 5' overhang, and either with or without TEV
238 protease and in the presence or absence of ATP. The unwinding of dsRNA to ssRNA was monitored
239 on a native polyacrylamide gel (Fig. 6A). This revealed that the release of 2C's N terminus from MBP
240 y the TEV protease was absolutely required for any RNA unwinding activity (Fig. 6A-B). With the N
241 terminus released, both 2C and 2C(41-329) showed partial RNA unwinding activity in the absence of
242 ATP, indicative of ATP-independent RNA chaperoning activity (Fig. 6A-B). However, the addition of
243 Mg^{2+}-ATP did not lead to increased unwinding of the dsRNA as expected from an RNA helicase. In
244 fact, the presence of Mg^{2+}-ATP instead led to less conversion of dsRNA to ssRNA (Fig. 6A-B). This
245 was consistent between full-length and truncated 2C, and the same was also seen when a dsRNA with
246 3' overhang was used (Fig. 6C-D). In stark contrast, when the ATPase activity of 2C was measured
247 under similar conditions, only the full-length protein was found to have appreciable ATPase activity,
248 and this was independent of whether it was fused to MBP, or if there was a membrane present (Fig.
249 6E). Notably, this correlates with the conditions for hexamerization of 2C (Fig. 2) but not with the
250 conditions under which 2C displayed RNA chaperoning activity (Fig. 6E). In summary, membrane-
251 bound full length 2C is an active ATPase, but its RNA chaperoning activity is not ATP-dependent.
252 The ATPase activity appears to correlate with the hexamerization of 2C, whereas the ATP-dependent
253 RNA chaperoning activity correlates with the liberation of its N-terminus.

254

255 **AH1 contributes to viral RNA replication to a similar degree as the entire MBD**

256 The biochemical reconstitution allowed us to study the separate contributions of AH1 and AH2 to
257 processes such as membrane binding and membrane clustering. To investigate their relative
258 contribution to viral RNA replication in cells, we used poliovirus replicons where the capsid proteins
259 were replaced by Renilla luciferase. As opposed to the biochemical experiments, the 2C truncations in
260 replicons (Δ(2-11) and Δ(2-40)) retained the staring glycine of 2C since it is a core part of the viral
261 protease 3C cleavage site (Fig. 7A). 12 hours after transfecting replicon RNAs into cells, they were
262 harvested, and the luciferase signal was quantified. The luminescence from both the Δ(2-11) and Δ(2-
263 40) replicons was significantly reduced, by approximately two orders of magnitude for the replicon
264 containing unaltered, full-length 2C. Thus, although AH1 appeared to have more subtle roles in the
265 biochemical experiments (e.g. in vesicle clustering), it is indispensable for effective viral RNA
266 replication in cells.

267

268 **Discussion**

269 With fewer than 7,000 coding nucleotides, the *Enterovirus* genome can sustain a full viral replication
270 cycle by encoding multifunctional proteins, and by hijacking host-cell functions. A universally present
271 and highly conserved enteroviral protein is the AAA+ ATPase 2C, whose suggested roles range from
272 membrane remodeling to RNA helicase and capsid morphogenesis. The nature of 2C as an
273 oligomerizing, peripheral membrane protein has impeded biochemical studies, that have typically been
274 conducted on truncated protein not engaging a membrane. Here we described the *in vitro*
275 reconstitution of purified, full-length 2C's binding to membranes. We used this more realistic, yet

276 completely defined, system to investigate several functions of 2C. In summary, our findings are
277 consistent with the model shown in Fig. 8.

278 We showed that the N-terminal MBD is divided into two amphipathic helix segments, AH1 and AH2,
279 separated by a highly conserved glycine residue (Fig. 1C, Fig. S1). AH2 appears to be the main
280 mediator of 2C's hexamerization in solution (Fig. 2), and is sufficient for membrane binding (Fig. 3C).
281 Of note, removal of the N-terminal maltose-binding protein (MBP) tag was not necessary for 2C to
282 bind membranes in our assay, but it was strictly required for 2C to recruit RNA to membranes (Fig.
283 5D), and for its RNA chaperoning activity (Fig. 6A). Whereas the N-terminal MBP tag is an artificial
284 addition to aid purification of recombinant 2C, the fusion of 2C's N-terminus to another protein is, in
285 fact, relevant to infection. 2C is initially excised from the viral polyprotein in the form of the stable
286 precursor 2BC, in which the N terminus of 2C is still fused to the viral protein 2B [57]. Hence, our
287 finding that 2C only binds RNA after its N terminus is liberated may be indicative of what happens in
288 an infected cell when 2BC is processed to 2B and 2C.

289 Our study revealed a novel role for 2C in clustering vesicles, a role mediated by AH1 (Fig. 4). This
290 finding suggest a biochemical mechanism for the 2C-mediated recruitment of lipid droplets to
291 replication organelles (ROs)[23]. 2C-mediated membrane clustering may also be involved in
292 generating the tightly stacked membrane tubes that make up the ROs at early time points [20, 58].
293 Notably, the deletion of AH1 led to a stark reduction of poliovirus genome replication, similar in
294 effect to the deletion of the entire MBD (Fig. 7). This may indicate that the lipid-clustering activity of
295 2C is central to enterovirus replication, although it cannot be ruled out that AH1 deletion also affects
296 other aspects of the replication such as polyprotein processing. The decrease in 2C-mediated
297 membrane clustering seen with increasing nucleic acid concentration (Fig. 5A-B) suggests a balance
298 between 2C's role in membrane clustering at early time points, and a preferential role in RNA
299 replication and particle assembly at later time points (Fig. 8). In this context, the ability of 2C to bind
300 membranes independent of curvature and lipid species (Fig. 3D-E) fits its multitude of roles in binding
301 to different types of RO membranes and lipid droplets.

302 The localization of viral RNA replication to RO membranes is well established, but the molecular
303 mechanism behind the localization is poorly understood. An electrostatic interaction between the viral
304 polymerase 3D and anionic lipids may be part of the mechanism[59]. Here, we show that 2C is able to
305 recruit and retain RNA at membranes, with a selectivity for dsRNA (Fig. 5D). Long double-stranded
306 segments are not prevalent amongst cellular RNAs, but it is the form of the viral template RNA while
307 replicated. Thus, 2C could selectively localize viral template RNA to the ROs. On the other hand, full-
308 length, membrane-bound 2C had no ATP-dependent RNA helicase activity, and only weak ATP-
309 independent RNA chaperone activity (Fig. 6A-D). This is in line with most previous studies on
310 truncated and membrane-free 2C, and with structural models of the 2C hexamer indicating that its
311 central pore would be too narrow and have an incompatible electrostatic potential to support RNA
312 translocation [40, 41, 44]. The conditions for 2C ATPase activity were different from the conditions
313 that permitted RNA chaperoning: effective ATPase activity required the MBD, but did not require
314 removal of the N-terminal MBP tag (Fig. 6E). One possible interpretation of these data is that 2C
315 ATPase activity requires hexamerization, whereas its RNA binding, and its weak RNA chaperoning
316 activity, requires a free N-terminus. A recent study found that MBD-deleted 2C has RNA-stimulated
317 ATPase activity, which would be consistent with the above interpretation of our data if assuming that
318 RNA engagement restores hexamerization of 2C(41-329). The convergence of our work and previous
319 studies in suggesting that 2C is not a helicase can be interpreted in the light of the reported dsRNA-
320 unwinding activity of the polymerase 3D [60].

321 Taken together, our reconstitution of 2C membrane binding allowed us to shed light on several
322 functions of 2C: it is able to bind vesicles with no apparent preference for curvature and lipid
323 composition, it can cluster vesicles, and selectively recruit dsRNA to their surface without possessing
324 helicase activity. In spite of this, major questions remain unanswered about the role of 2C in

325 enterovirus RNA replication and particle assembly. Nothing is known about the supramolecular
326 arrangement of the RNA replication machinery on membranes, for instance how 2C, the polymerase
327 3D and host RNA-binding proteins such as PCBP1/2 are arranged [61]. Also, 2C is known to play a
328 role in capsid assembly and is suggested to be part of a "tether complex" enabling the RNA loading of
329 new capsids on RO membranes [19, 58], but biochemical mechanisms underlying this process are
330 largely unknown. The reconstitution of 2C-decorated vesicles presented here is a stepping stone
331 towards a more complete *in vitro* reconstitution of such complex processes.

332

333 **Materials and methods**

334 **Expression and purification of poliovirus 2C**

335 A codon-optimized synthetic gene corresponding to full-length 2C from poliovirus type 1 Mahoney
336 (GenBank: V01149.1) was inserted into 1M expression plasmid from Macrolab (University of
337 California, Berkeley, USA) with a TEV protease-cleavable, N-terminal His_6-MBP tag. The plasmid
338 was transformed to *E. coli* BL21(DE3) competent cells and grown overnight on LB-agar plates
339 containing 50ug/ml Kanamycin (KAN). A single colony was used to inoculate LB/KAN media, this
340 primary culture was grown for 5 hours. Then, a one-liter culture of LB/KAN was inoculated with 1ml
341 of the primary culture. The cells were grown at 37°C, induced at OD_{600}=2 by the addition of 0.5 mM
342 isopropyl-beta-D-thiogalacopyranoside, then incubated overnight at 25°C. Cells were collected by
343 centrifugation, and resuspended in lysis buffer (50 mM Tris, pH 8.5), 500 mM NaCl, 20 mM
344 Imidazole, 10% (v/v) glycerol, 36 µM NP40, 5 mM $MgCl_2$, 0.1 mM THP) containing protease
345 inhibitor cocktail (40 mM Phenylmethylsulfonyl fluoride, 1 mM Leupeptin and 200 mM Benzamidine
346 HCl) and DNase. The cells were lysed using a continuous flow cell disruptor (Constant Systems). The
347 lysate was cleared by centrifugation at 63,000*g at 4°C for 1 hour and the supernatant was loaded onto
348 Ni-NTA (nitrilotriacetic acid) resin and eluted with elution buffer (50 mM Tris (pH 8.5), 500 mM
349 NaCl, 250 mM Imidazole, 10% (v/v) glycerol, 36 µM NP40, 5mM $MgCl_2$, 0.1 mM THP). The protein
350 was then loaded onto a HiTrap Q HP Column (GE Healthcare) and eluted using a gradient from buffer
351 QA (50 mM Tris, pH 8.5), 50 mM NaCl, 10% (v/v) glycerol, 36 µM NP40, 5 mM $MgCl_2$, 0.1 mM
352 THP) and buffer QB (50 mM Tris (pH 8.5), 1 M NaCl, 10% (v/v) glycerol, 36 µM NP40, 5 mM
353 $MgCl_2$, 0.1 mM THP). The fractions containing the protein was loaded onto a 24 ml Superose 6
354 Increase 10/300 GL (Cytiva) that was equilibrated with SEC buffer (50 mM Tris-HCl (pH 7.4), 150
355 mM potassium acetate, and 0.1 mM THP). Purified 2C was then aliquoted, flash frozen with liquid N_2,
356 and stored at -80°C. All the other constructs of the protein were purified in a similar way.

357 To prepare 2C(41-329) and 2C(116-329) without His_6-MBP tag, the tagged proteins were diluted to
358 0.1mg/ml after the HiTrap Q HP column using buffer QA described above and the proteins were
359 cleaved at 4°C overnight by adding TEV protease in a molar ration TEV:2C of 1: 5 and 1:15 for
360 2C(41-329) and 2C(116-329), respectively. Uncleaved protein and His_6-MBP were removed by
361 incubating the mixture with NiNTA resin followed by passing of the protein over a 1ml MBPTrap
362 (Cytiva) column and then a HiTrap Heparin HP (Cytiva) using buffer QA and QB. The fractions
363 containing the protein were loaded onto a Superdex 75 Increase 10/300 GL (Cytiva) equilibrated with
364 SEC buffer. Purified cleaved 2C was aliquoted, flash frozen with liquid N_2, and stored at -80°C.

365 **Fluorophore labeling of proteins**

366 To label the proteins, after the HiTrap Q HP Column, the proteins were incubated with an equimolar
367 amount of Atto488 maleimide (Sigma-Aldrich) at 4°C overnight. Next day, excess dye was quenched
368 using 25 mM Dithiothreitol (DTT) and the proteins were loaded onto a Superose 6 Increase 10/300 GL
369 (Cytiva) column, pooled and snap frozen as described above for unlabeled protein. The labeling
370 efficiency was estimated by measuring the absorption of the labeled protein at 280 nm and at the
371 fluorophore absorption maximum. It was typically 0.5-1.1 fluorophores/2C monomer.

372 **SEC-MALS**

373 All the samples were run on an ÄKTA Pure (Cytiva) with a Superdex 200 Increase 10/300 GL
374 column, equilibrated in SEC buffer, coupled to a light scattering (Wyatt Treas II) and refractive index
375 (Wyatt Optilab T-Rex) detector. Bovine serum albumin (BSA) was used to calibrate the system. 150
376 to 500 µl (0.6 to 1 mg/ml) of protein was injected at a flow rate of 400 µl/min. Data were analyzed
377 using Astra software (version 7.2.2; Wyatt Technology).

378 **Mass photometry**

379 Proteins were diluted to 100 nM in 50 mM Tris pH 7.4 and applied to a glass coverslip and recorded
380 on Mass Photometer[62] (OneMP, Refeyn Ltd) for 60 seconds. The data were analyzed using
381 DiscoverMP (Refeyn Ltd) and the molecular weight was obtained by contrast comparison with known
382 mass standards measured on the same day and were repeated three times, and visualized as mean +/-
383 standard deviation.

384 **Multiple sequence alignment**

385 Multiple sequence alignment of amino acids 1-40 was performed on EV71 (GenBank: AAB39969.1),
386 CVB3 (GenBank: AFD33642.1), PV type 1 (MAHONEY STRAIN) (GenBank: V01148.1), EV D68
387 (GenBank: ALE66301.1), RV A2 STRAIN USA/2018/CA-RGDS-1062 (GenBank: MN228695.1) and
388 RV C15 (GenBank: ACZ67658.1) using Clustal Omega[63] with default parameters.

389 **Amphipathic helix prediction**

390 The physicochemical properties 2C amino acids 1-40 from EV71 (GenBank: AAB39969.1), CVB3
391 (GenBank: AFD33642.1), PV type 1 (Mahoney strain) (GenBank: V01148.1), EV D68 (GenBank:
392 ALE66301.1), RV A2 STRAIN USA/2018/CA-RGDS-1062 (GenBank: MN228695.1) and RV C15
393 (GenBank: ACZ67658.1) were determined using heliquest (https://heliquest.ipmc.cnrs.fr/) [64] using
394 alpha-helix as helix type and window size of one turn (18 residues). The mean amphipathic moment or
395 transverse hydrophobic moment (µH) was plotted against the amino acid at the center of the analysis
396 window.

397 **Structure predictions**

398 All structures were predicted using Alphafold 2 implemented in COLABFOLD
399 ((https://colab.research.google.com/github/sokrypton/ColabFold/blob/main/AlphaFold2.ipynb) [49]
400 with default settings. The cartoon representations were generated using CHIMERAX [50].

401 **Preparation of small unilamellar vesicles (SUVs)**

402 1-palmitoyl-2-oleoyl-sn-glycero-3-phospho-L-serine (POPS), 1-palmitoyl-2-oleoyl-sn-glycero-3-
403 phosphoethanolamine (POPE) and 1-palmitoyl-2-oleoyl-sn-glycero-3-phosphocholine (POPC) were
404 purchased from Avanti Polar lipids. Total 1 mg/ml of lipids containing POPC (25 mol %), POPE (25
405 mol %), POPS (25 mol %) or POPC (75 mol %), POPE (25 mol %), and 1, 2-Dioleoyl-sn-glycero-3-
406 phosphoethanolamine labeled with Atto 647N (0.1 mol %) was dried onto a borosilicate glass tube
407 wall with a nitrogen stream and kept overnight in vacuum desiccator for complete removal of solvents.
408 500 µl of SEC buffer was added into the mixture. The tube was then vortexed to resuspend the lipids
409 and then, kept in a water bath at 42°C for 15 min. Then, the lipids were transferred to an Eppendorf
410 tube for sonicating with a tip sonicator (10 seconds pulse, 20 seconds rest, and 20% amplitude) until a
411 clear solution was observed. Then, the tube was centrifuged at 21,000*g at 4°C for 20 min. Then, 300
412 µl of supernatant was carefully removed, and the quality of the preparation was checked using
413 dynamic light scattering as described below. SUVs were kept at 4°C until use, at most for 3 days.

414 **Preparation of large unilamellar vesicles (LUVs)**

415 Total 1 mg/ml of lipids containing POPC (75 mol %), POPE (25 mol %) and1, 2-Dioleoyl-sn-glycero-
416 3-phosphoethanolamine labeled with Atto 647N (0.1 mol %) was dried onto a borosilicate glass tube
417 wall with a nitrogen stream and kept overnight in vacuum desiccator. Then, 500 µl of SEC buffer was
418 added into the mixture. The tube was then vortexed to resuspend the lipids and to break the multi-
419 lamellar vesicles, the lipids were subjected to 12 freeze-thaw cycles by moving it between a 42°C
420 water bath and liquid nitrogen. Then, this solution was passed 21 times through an extrusion
421 membrane (Whatman Nuclepore) with pore size of 2 µm on a mini-extruder (Avanti Polar Lipids) to
422 get a clear solution comprising of LUVs. The quality of the preparation was checked using Dynamic
423 light scattering as described below. LUVs were kept at 4°C until use, at most for 3 days.

424 **Vesicle flotation assay**

425 A reaction mixture of 100 µl was prepared containing 0.8 µM Atto488 maleimide His_6MBP-2C, 1
426 mg/ml SUVs or LUVs and X µM TEV protease was incubated for 2 hours at room temperature. Then,
427 this reaction mixture was mixed with 500 µl of 48% (w/v) OptiPrep density gradient medium (Merck
428 (Sigma-Aldrich)) and this mixture was carefully placed at the bottom of an Open-Top Thin wall Ultra-
429 Clear Tube (Beckman Coulter) and was overlaid with 800 µl of 30% (w/v) OptiPrep followed by
430 another layer of 800 µl of 20% (w/v) OptiPrep and finally 2 ml of SEC buffer. The tubes were then
431 ultra-centrifuged at 364,000*g for 3 hours at 4°C. After centrifugation different fractions were
432 carefully taken out from the tubes and fluorescence was measured using Agilent BioTek Synergy
433 fluorimeter.

434 **Flotation assay with fluorescently labeled RNA**

435 All oligonucleotides used in this study are listed in Table 1. 100 µl of reaction mixture was prepared as
436 described above, except that unlabeled 2C was used, and a final concentration of 500 nM of single-
437 stranded 5' TET-labeled RNA(5'CCUCUAACCACAGUCUGAUC 3') (Eurofins Genomics) or
438 dsRNA (described below) was added. The flotation assay was performed as described above and the
439 TET fluorescence was measured. To prepare dsRNA, 10uM of 5' TET labelled RNA
440 (5'CCUCUAACCACAGUCUGAUC 3') was mixed with its 10uM unlabeled complementary strand
441 in a buffer containing 50mM HEPES pH7.2, 100mM KCl and RNase secure. The mixture was heated
442 to 95°C and then the temperature was decreased by 0.5°C /minute until 22°C. The annealed dsRNA
443 was then placed overnight at 4°C and then at -20°C until use. The extent of annealing was checked
444 using a 16% acrylamide non-denaturing RNA gel. A standard curve was prepared using fluorescence
445 reading for ssRNA and dsRNA and the extent of binding of RNA to 2C was quantified using this
446 standard curve.

447 **Dynamic light scattering**

448 100 µl of reaction mixture was prepared containing 0.8 µM or 3 µM 2C, 1 mg/ml SUVs, and TEV
449 protease was incubated for 30 min at room temperature. Then, this mixture was transferred into a
450 cuvette and the particle size was determined by dynamic light scattering using a Zetasizer Nano-ZS
451 (Malvern Instruments, Worcestershire, UK) at room temperature. To check the effect of ssDNA on
452 clustering, increasing concentration of ssDNA oligo (5' TGAATGCGGCTAATCCCAACCT 3')
453 (Eurofins Genomics) was added in to the mix containing TEV protease, 1 mg/ml SUVs followed by
454 addition of protein and the particle size was determined as described above.

455 **Sample preparation for cryo-electron tomography**

456 A reaction mixture of 100 µl was prepared containing 3 µM His_6MBP-2C, 1 mg/ml SUVs and 4 µM
457 TEV protease was incubated for 30 min at room temperature. 3 µl of this mixture was blotted on a
458 glow-discharged Quantifoil R 2/1 Copper 300 mesh grid (Electron Microscopy Sciences) and plunge-
459 frozen in liquid ethane using a Vitrobot plunge freezer (ThermoFisher Scientific) at 22°C, 80%
460 humidity, with blot force -20, blot time 2 seconds and wait time 40 seconds.

461 **Cryo-electron tomography data collection and processing**

462 Tomographic tilt series were collected using a Titan Krios (ThermoFisher Scientific) operated at 300
463 kV, with a 100 µm objective aperture, Selectris energy filter and Falcon 4i detector (ThermoFisher
464 Scientific). Tilt series were acquired in dose-symmetric mode, using SerialEM version 4. The
465 following parameters were used for acquisition: 26,000 x nominal magnification corresponding to a
466 specimen pixel size of 4.7 Å; defocus range of -3 µm to -8 µm, ± 63° tilt-range with tilt increment of
467 3°; total electron dose ~116 $e^-/Å^2$. At each tilt angle, the exposure was saved as an EER movie. The
468 EER files were converted to TIFF files using IMOD [65], gain-reference corrected, and motion
469 corrected using MotionCor2 [66]. The tilt series were then processed and aligned using IMOD[65].
470 CTF was estimated using CTFFIND4 [67] and corrected using phase flipping as implemented in
471 IMOD's CTFPHASEFLIP.

472 The isotropic resolution and signal-to noise ratio of the tomograms were improved using the de-
473 noising deep-learning software IsoNet [68]. The filtered tomograms were used for segmentation using
474 Amira (Thermo Fisher Scientific) for the representation of SUVs and 2C.

475 **Colorimetric ATPase assay**

476 Malachite Green Phosphate Assay Kit (MAK307, Sigma-Aldrich) was used for the colorimetric
477 ATPase assay. For the enzymatic reaction 1.2 µM of His_6MBP-2C (1-329) or (41-329), 2.9 µM TEV
478 protease, 0.5 mg/ml SUV (POPC (25 mol %), POPE (25 mol %) and 0.4 mM ATP was mixed in
479 buffer containing 40 mM HEPES pH7.5, 2 mM DTT and 12 mM NaCl and was incubated for 2 hours
480 at 37 °C. The samples were diluted 20 times and plated in a 96 well plate and mixed with 20 µl
481 working reagent supplied with the kit. The mixture was incubated at 37°C for 30 min after which the
482 absorbance was measured at 620 nm according to manufacturer's instructions. A standard curved was
483 prepared using the provided standard phosphate in same buffer as the reaction. This standard curve
484 was used to determine the phosphate liberated in the ATPase assay.

485

486 **Double-stranded RNA unwinding assay**

487 The single stranded RNA (ssRNA) oligos (Eurofins Genomics) were annealed in molar ratio 1:1.5 (28
488 nucleotide labeled oligomer (5' AAAAAAAAAAAACCAGGCGACAUCAGCG-FAM3'): 16
489 oligomer un-labeled (5'CGCUGAUGUCGCCUGG3')) in a buffer containing 10 mM HEPES-NaOH
490 (pH 7.2) and 10 mM KCl. This mix was heated to 95°C for 1 minute and then cooled down to 22°C at
491 the rate of 1°C per minute. The sample was then kept at 22°C for one hour. The thus prepared dsRNA
492 with 5' overhang was kept at 4°C overnight before freezing at -20°C. The dsRNA with 3' overhang
493 was made similarly using 28 nucleotide labeled oligomer (FAM-
494 5'CCAGGCGACAUCAGCGAAAAAAAAAAAA3') and mixing with 16 oligomer un-labeled
495 (5'CGCUGAUGUCGCCUGG3'). Chaperone activity assay was performed in reaction buffer
496 containing 40 mM HEPES pH7.5, 2 mM DTT and 15mM NaCl, 0.5 µl RNAse inhibitor, 0.8 mg/ml of
497 SUVs (POPC (25 mol %), POPE (25 mol %) (the SUVs were prepared using the reaction buffer), 1.2
498 µM MBP-2C , 3.8 µM of TEV protease, 40 nM dsRNA template, 800 nM ssRNA trap strand (28
499 nucleotide un-labeled oligomer). This mixture was incubated at 37°C for 20 min, followed by addition
500 of 3.5 mM magnesium-ATP to start the reaction. The reaction was incubated for 2 hours before adding
501 5 µl of quenching buffer consisting of 100 mM Tris pH 7.5, 0.1% bromophenol blue, 1% SDS, 50 mM
502 EDTA, and 50% glycerol. The samples were run on 16% native polyacrylamide gels for 2 hours at
503 100 V and scanned using an Amersham Typhoon fluorescence gel scanner. The gel scans were
504 quantified using ImageJ, measuring the intensity of the bands at the ssRNA position as defined by the
505 ssRNA control and subtracting the intensity of the dsRNA control as background.

506

507 **Luciferase assay**

508 The P2-P3 region from poliovirus type 1 Mahoney (GenBank: V01149.1) was inserted into a vector
509 containing *Renilla* luciferase reporter on the N-terminus. Truncated 2C versions (Δ2-11 and Δ2-40)
510 were also constructed. The first glycine residue of 2C was not truncated in order to preserve the 3C
511 protease cleavage site. The plasmids were linearized using ApaI restriction enzyme followed by *in*
512 *vitro* transcription using MEGAscript™ T7 Transcription Kit (Invitrogen) according to manufacturer's
513 protocol. The quality of the RNA was checked using 0.5% denaturing agarose gel. For transfection, 1
514 µg RNA was used and transfected in HeLa cells using TransIT®-mRNA Transfection Kit (mirusbio)
515 according to manufacturer's instruction. The cells were harvested for luciferase assay after incubation
516 at 37°C for 12 hrs. The same procedure was repeated for GFP-CVB3 replicon RNA which was used as
517 transfection control (negative control for luciferase signal). The cells were lysed using lysis buffer
518 supplied with Renilla Luciferase Assay Kit 2.0 (Biotium). 20 µl of cell lysate was mixed with 100 µl
519 of freshly prepared working solution and the luminescence was recorded using a TECAN
520 spectrophotometer.

521

522 **Graphs and statistical procedure**

523 Statistical significance tests were performed using student's T-test as implemented in GraphPad Prism
524 v10.0.1. Error bars represent standard deviation. P value style: ; ns: $p > 0.05$; ; *: $p < 0.05$; **: $p < 0.01$;
525 ***: $p < 0.001$; ****: $p < 0.0001$

526

527 **Data availability**

528 The cryo-electron tomogram shown in Fig. 4C has been deposited to the Electron Microscopy Data
529 Bank with accession code EMD-XXXXX.

530 **Acknowledgements**

531 We would like to thank Madeleine Ramstedt (Department of Chemistry, Umeå University) for the
532 introduction to the Zetasizer Malvern Nanoz used for DLS measurements and Mikael Lindberg
533 (Protein expertise platform, Umeå University, part of Protein Production Sweden) for cloning the
534 poliovirus replicons. Cryo-ET was performed at the Umeå Center for Electron Microscopy (UCEM) a
535 SciLifeLab National Cryo-EM facility part of the National Microscopy Infrastructure, NMI (VR-RFI
536 2016–00968). This project was funded by a Human Frontier Science Program Career Development
537 Award (CDA00047/2017 C) to LAC, a Kempe foundations postdoctoral fellowship to MNS, an
538 MSCA fellowship to HS ("MsInfection", grant agreement ID: 101033469), the Knut and Alice
539 Wallenberg Foundation (through the Wallenberg Center for Molecular Medicine Umeå), and the
540 Swedish research council (grants 2018–05851 and 2021–01145).

541

Figures and Tables

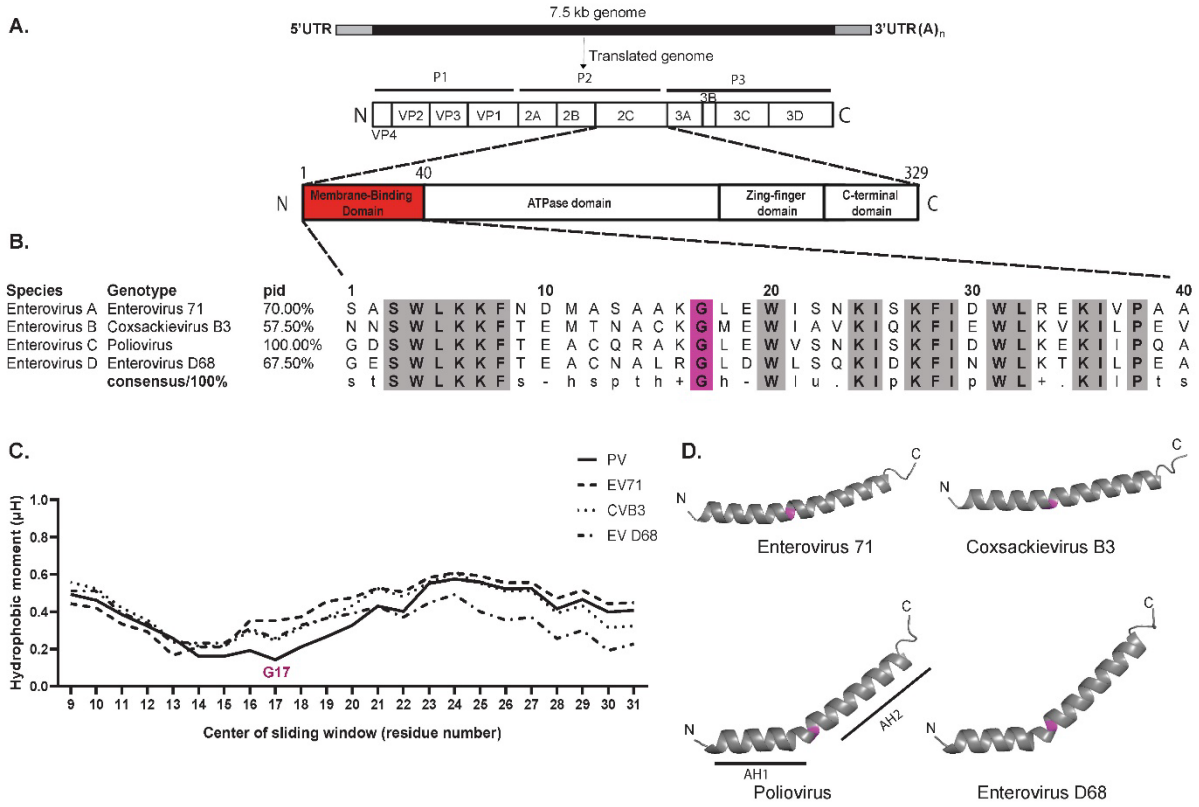

Figure 1: The membrane-binding region of 2C consists of two amphipathic helix regions, separated by a conserved glycine. (A) Schematic representation of the *Enterovirus* genome, the translated polyprotein with individual proteins marked, and the 2C protein with known domains marked. **(B)** Multiple sequence alignment of the membrane-binding domain (MBD, residues 1-40) of 2C from representative genotypes of different *Enterovirus* species. Conserved polar and hydrophobic residues are highlighted in grey (s: small residue, t: turn like residue, h: hydrophobic residue, p: polar residue, l: aliphatic residue, +: positively charged residue, -: negatively charged residue). The conserved glycine (number 17 in poliovirus 2C) is highlighted in pink. **(C)** Hydrophobic moment (μH), a measure of the local amphiphilicity of a helix in a 18-residue sliding window, is plotted for representative genotypes of different enterovirus species. The higher the μH value, the more an amphipathic the helix at that position. The position of the conserved glycine 17 is marked. **(D)** Alphafold2 structure prediction of the MBD of 2C from representative genotypes of different enterovirus species. The conserved glycine 17 is highlighted in pink separating AH1 and AH2.

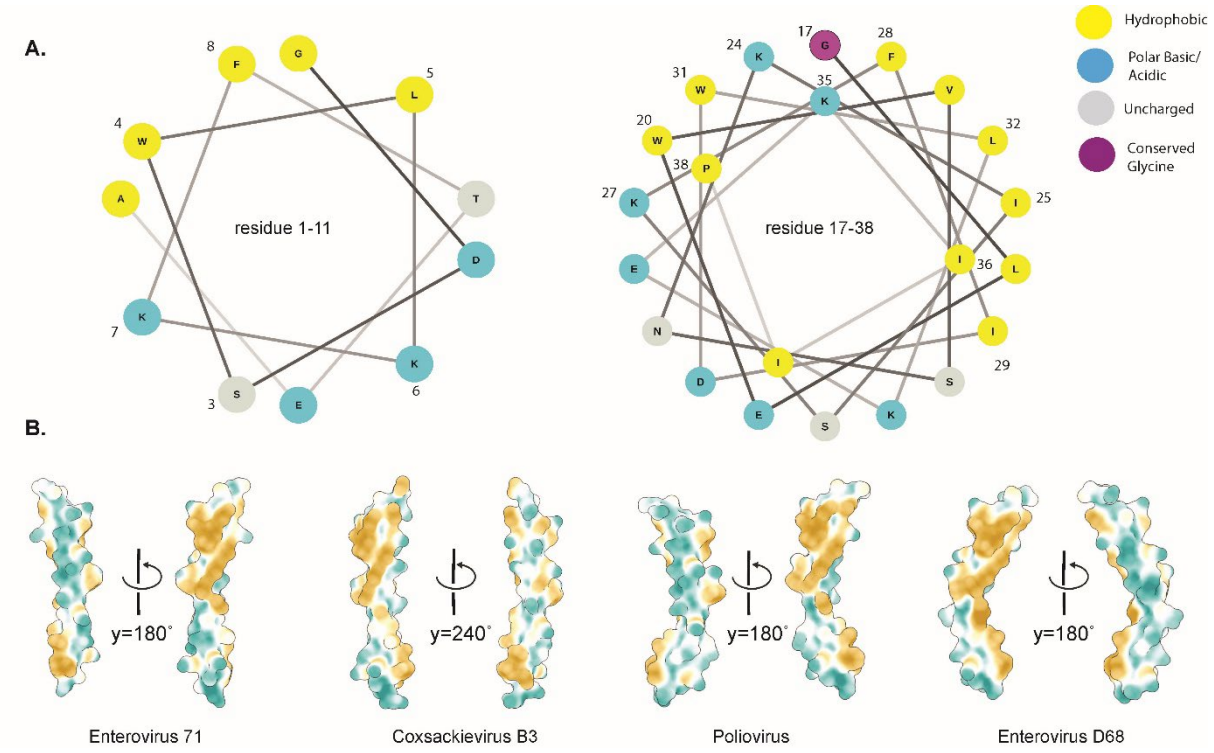

Figure S1: Amphipathic nature of the 2C membrane-binding domain. (A) Helical wheel of the AH1 and AH2 regions of poliovirus type 1 Mahoney 2C (GenBank: V01148.1) showing the distribution of hydrophobic and hydrophilic residues. Conserved residues are numbered. **(B)** Isosurface representations of Alphafold2-predicted structures of the MBD of different enterovirus genotypes showing the distribution of hydrophilic (blue) and hydrophobic (yellow) residues. For each structure prediction, two views related by the indicated rotation are shown.

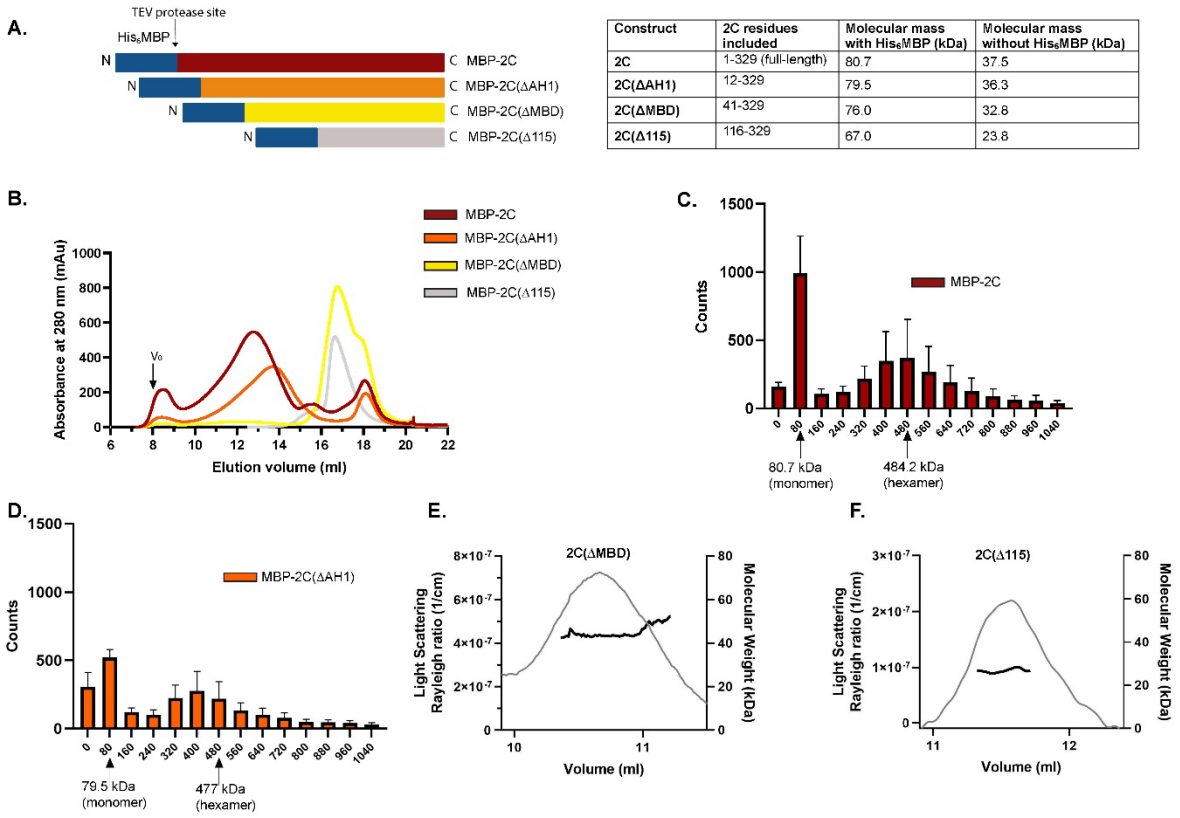

Construct	2C residues included	Molecular mass with His_6MBP (kDa)	Molecular mass without His_6MBP (kDa)
2C	1-329 (full-length)	80.7	37.5
2C(ΔAH1)	12-329	79.5	36.3
2C(ΔMBD)	41-329	76.0	32.8
2C(Δ115)	116-329	67.0	23.8

Figure 2: The membrane-binding domain regulates 2C oligomerization. (A) Schematic representation of all the His_6-MBP-(TEV) constructs used in the paper: full-length 2C, and N-terminally truncated versions: 2C(ΔAH1) corresponding to deletion of AH1, 2C(41-329) corresponding to deletion of AH1-2 (entire MBD), and 2C(116-329) corresponding to deletion of MBD and part of the ATPase domain (comparable to published crystal structure)[39]. **(B)** Elution profile of the constructs described in panel A on a Superose 6 Increase size-exclusion column. The peaks were centered at the following elution volumes: 12.5 ml for MBP-2C, 13.5 ml for MBP-2C(ΔAH1), 16.5 ml for MBP-2C(41-329), and 17.0 ml for MBP-2C(116-329). The column void volume is indicated with V_0. **(C-D)** Mass photometry data showing the molecular mass distribution at 100 nM concentration of C: MBP-2C(ΔAH1) and D: MBP-2C(ΔAH1). Error bars represent a standard deviation of three repeats of the experiment. **(E-F)** SEC-MALS data showing estimated molecular mass of MBP-free 2C(41-329) and 2C(116-329) at concentrations of 38 and 134 μM, respectively. Throughout the main elution peak, 2C(41-329) had an estimated mass of 43 and 52 kDa for two consecutive runs, whereas 2C(116-329) had an estimated mass of 22 and 27 kDa for two consecutive runs.

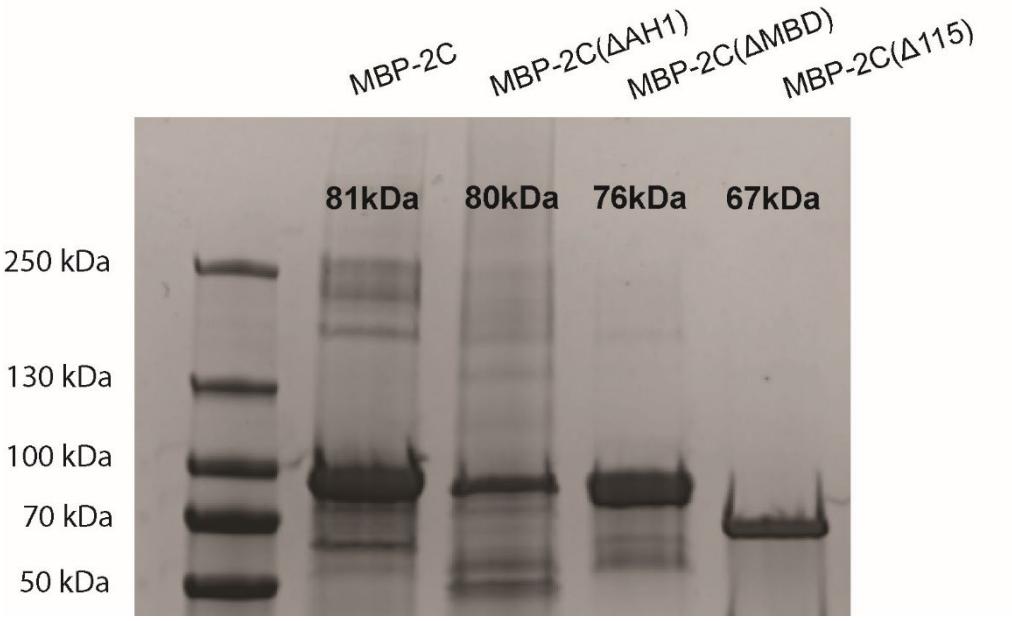

Figure S2: SDS PAGE gel showing different 2C constructs. lane 1: molecular mass ladder with masses indicated to its left. lane 2: His_6-MBP-(TEV)-full-length 2C, and N-terminally truncated versions: lane 3: His_6-MBP-(TEV)-2C(ΔAH1), lane 4: His_6-MBP-(TEV)-2C(41-329), and lane 5: His_6-MBP-(TEV)-2C(116-329).

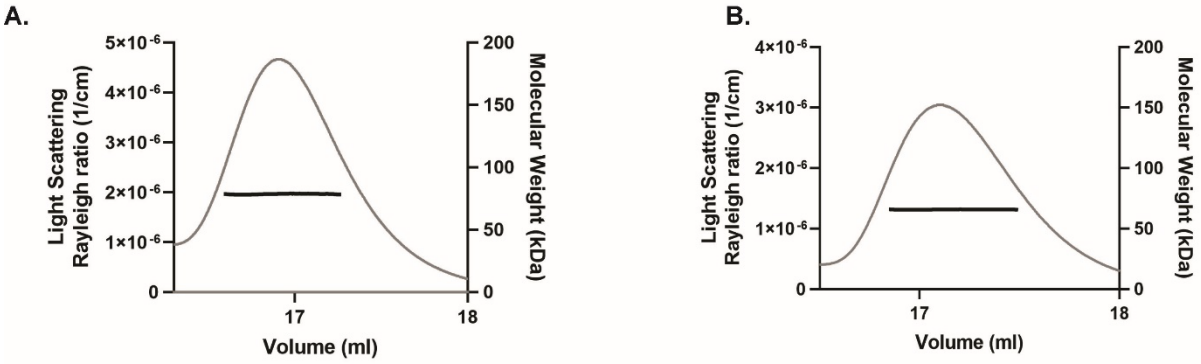

Figure S3: SEC-MALS mass analysis of MBP-fused truncated 2C constructs. SEC-MALS data showing estimated molecular mass throughout the main elution peak of (**A**) MBP-2C(41-329) and (**B**) MBP-2C(116-329) at concentrations of 38 and 134µM, respectively. The calculated masses are shown as a thick black line. MBP-2C(41-329) had an estimated mass of 78 kDa, whereas MBP-2C(116-329) had an estimated mass of 66 kDa.

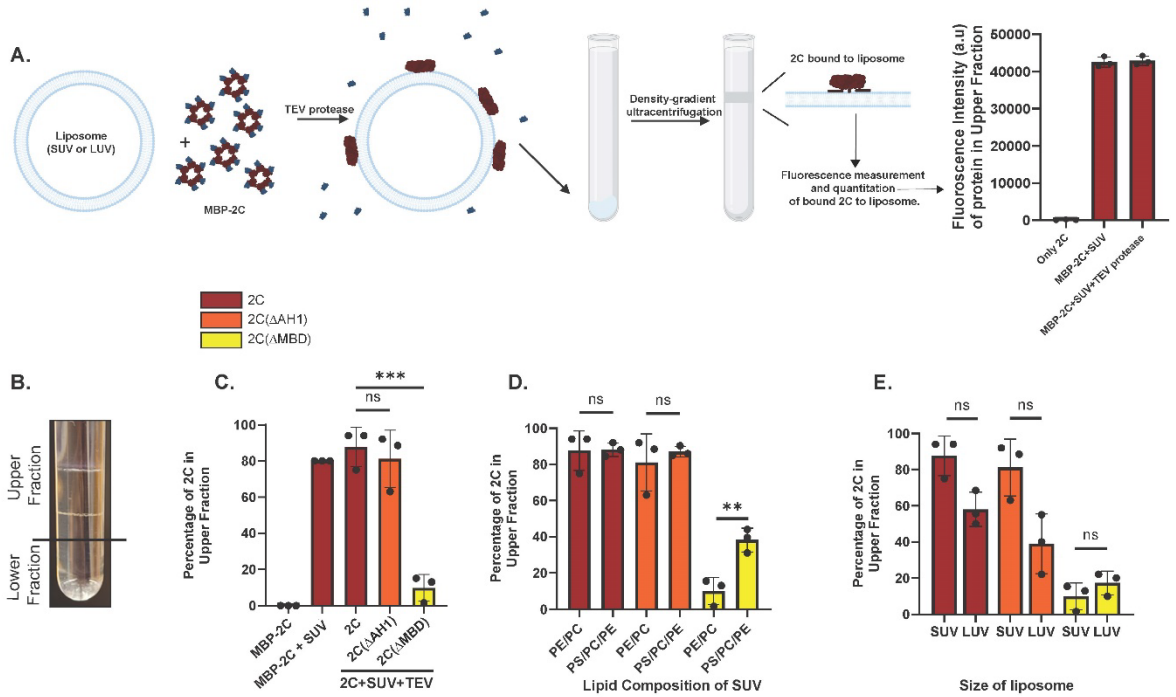

591

592 **Figure 3: The AH2 region is critical for 2C's membrane binding. (A)** Schematic representation of the
593 flotation assay used to quantify the membrane binding property of 2C. MBP-2C is fluorophore-labeled with
594 ATTO488 on exposed cysteines, which only exist in the 2C part of the fusion protein. Small unilamellar vesicles
595 (SUVs) or large unilamellar vesicles (LUVs) – collectively: liposomes – are labelled with DOPE-coupled
596 ATTO647N, thus having a distinct fluorescence signal from the protein. The MBP tag is cleaved from MBP-2C
597 using TEV protease in the presence of liposomes, allowing the liberated MBD to directly associate with the
598 liposomes. 2C-decorated liposomes are layered at the bottom of a density gradient and subjected to ultra-
599 centrifugation. The amount of liposomes present in the top fraction, and their bound 2C, is quantified in separate
600 channels of a fluorimeter. 2C hexamers are dark red, MBP blue. **(B)** Photograph of a representative centrifuge
601 tube after the flotation assay with 2C, showing two distinct lipid bands in the upper fraction. **(C)** Flotation assays
602 were conducted as shown in panel A, with SUVs composed of 75 mol% POPC and 25 mol% POPE, having an
603 average diameter of typically ~50 nm as measured by DLS. 2C fluorescence was measured separately in upper
604 and lower fractions, and the percentage present in the upper fraction is plotted for the different 2C constructs.
605 Error bars represent a standard deviation of three repeats of the experiment. Statistical significance by unpaired
606 two-tailed Student's t test; ns > 0.05; ***$p < 0.001$. **(D)** Flotation assay as in C, but with varying SUV lipid
607 composition. PE/PC: 25 mol% POPC, 75 mol% POPE. PE/PC/PS: 25 mol% POPC, 25 mol% POPE, 50 mol%
608 POPS. Error bars represent a standard deviation of three repeats of the experiment. Statistical significance by
609 unpaired two-tailed Student's t test; ns >0.05; **$p < 0.01$. **(E)** Flotation assay as in C, but with varying liposome
610 size. SUV: sonicated SUVs, ~50 nm diameter. LUV: extruded LUVs, ~2500 nm diameter. Error bars represent a
611 standard deviation of three repeats of the experiment. Statistical significance by unpaired two-tailed Student's t-
612 test; ns > 0.05.

613

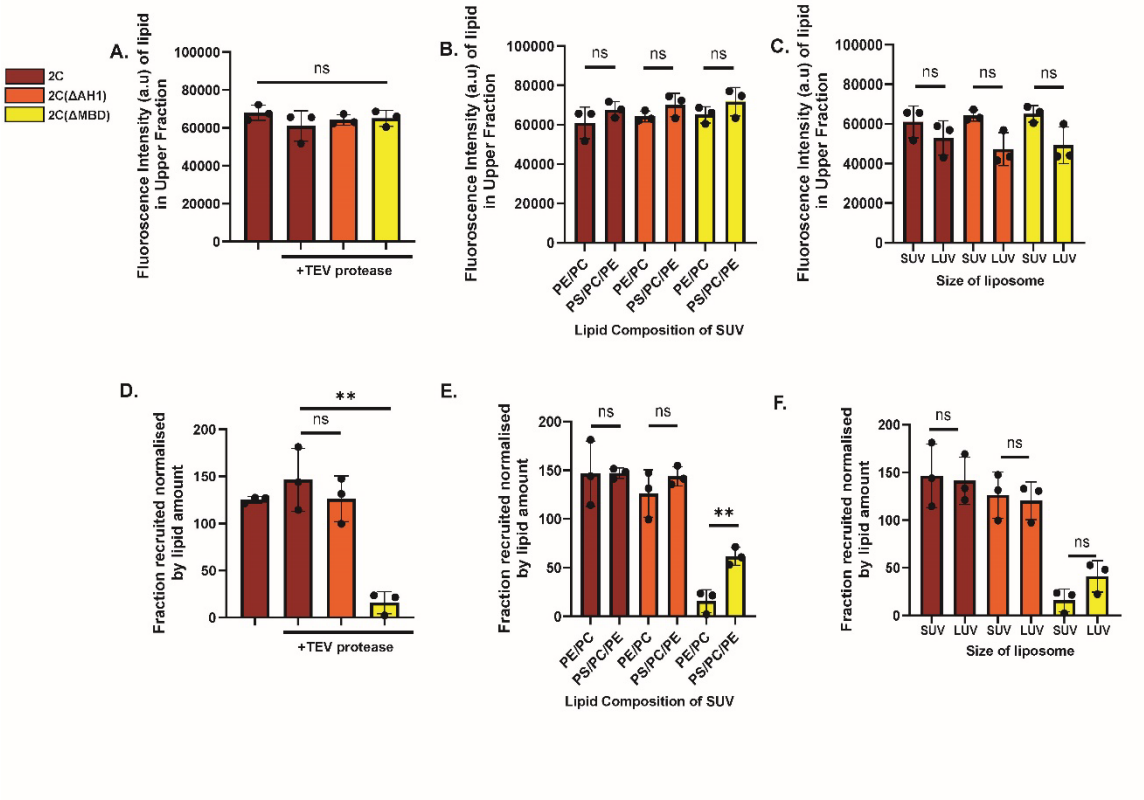

Figure S4: Quantitation of lipid fluorescence in flotation experiments. (A-C) Lipid fluorescence signal in the upper fraction of the assays shown in Fig. 3C-E. Error bars represent a standard deviation of three repeats of the experiment. Statistical significance by unpaired two-tailed Student's t test; ns > 0.05. (**D-E**) Fraction 2C recruited to the upper fraction, normalized by amount of lipid in the upper fraction, for the assays shown in Fig. 3C-E. Error bars represent a standard deviation of three repeats of the experiment. Statistical significance by unpaired two-tailed Student's t-test; ns > 0.05; **p < 0.01.

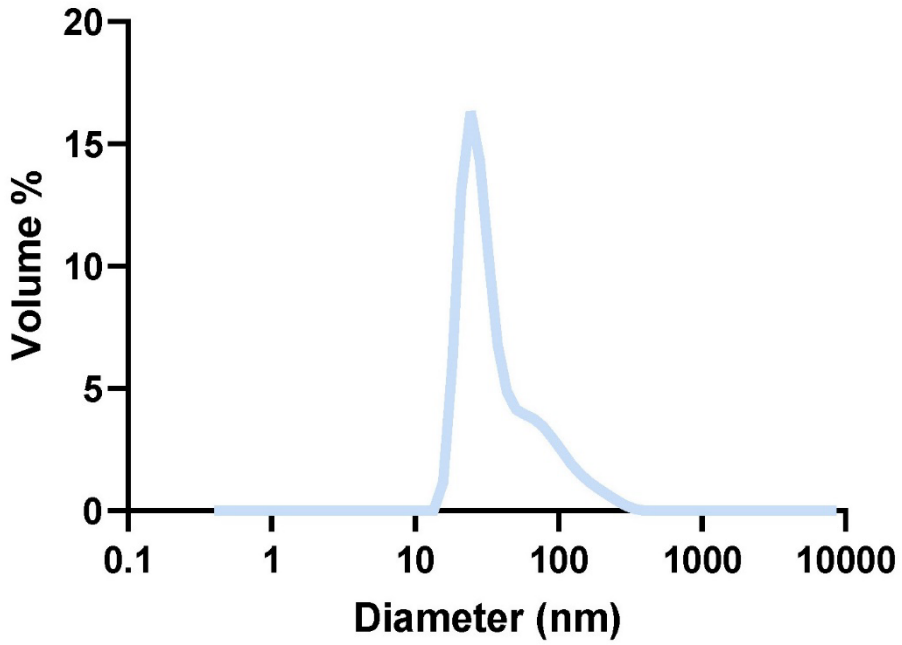

Figure S5: Size distribution of SUVs. Dynamic light scattering graph showing the size distribution of PE/PC SUV (size distribution by volume). Average size of the SUVs was calculated to be 30 nm.

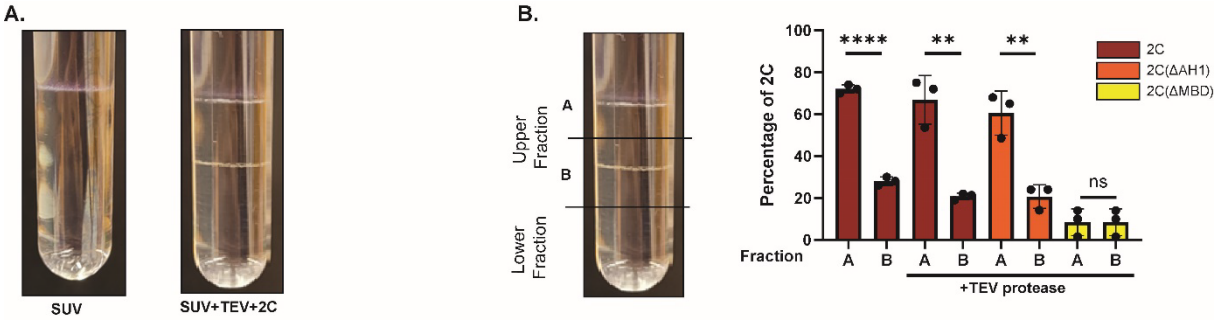

Figure S6: Two distinct lipid bands in the upper fraction in 2C flotation assays. (A) Photograph of representative centrifuge tubes after the flotation assay with SUVs only (single lipid band), and SUVs + TEV protease + MBP-2C (two lipid bands). **(B)** Photograph of centrifuge tube, indicating the upper fractions A, B, and the lower fraction. The percentage of the total 2C fluorescence in fractions A and B are shown. Error bars represent the standard deviation of three repeats of the experiment. Statistical significance by unpaired two-tailed Student's t-test; $^{**}p < 0.01$; $^{****}p < 0.0001$.

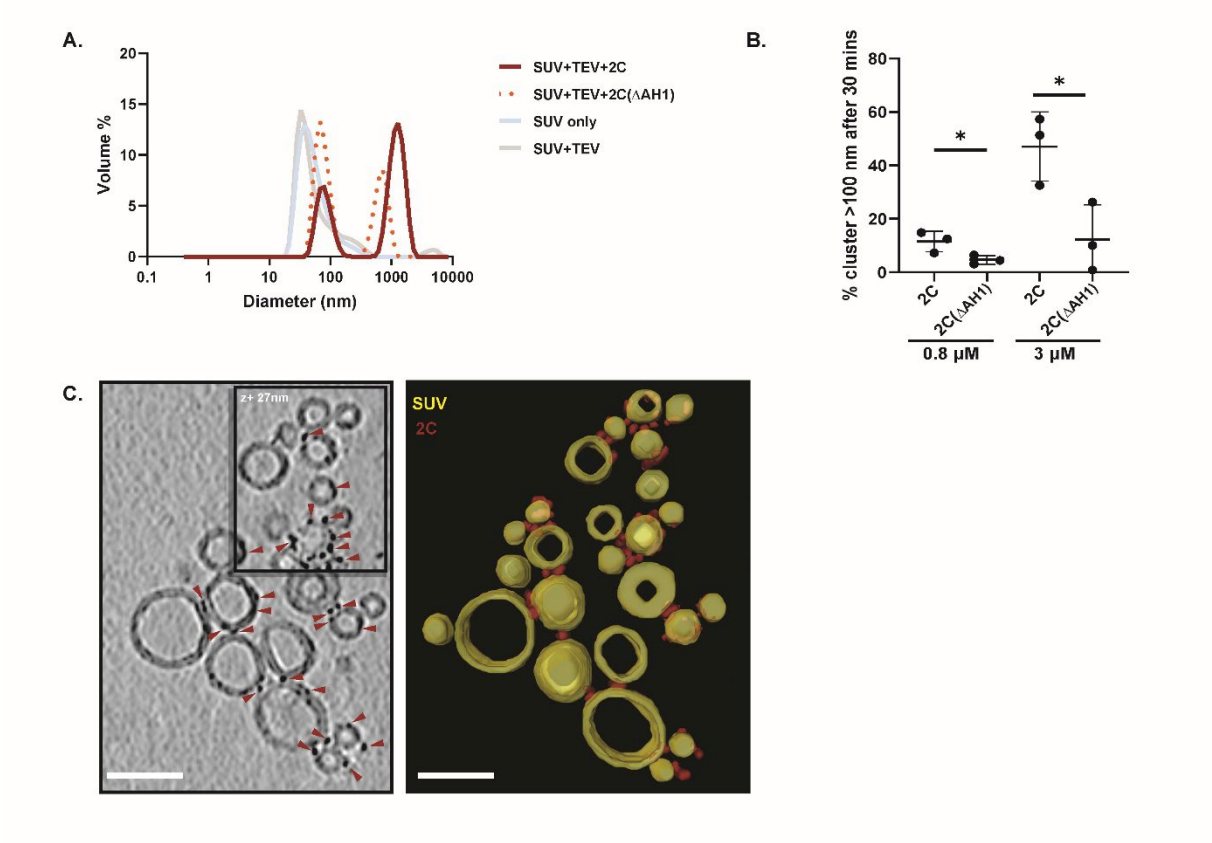

Figure 4: 2C has lipid clustering activity that is enhanced by the AH1 region. (A) Representative dynamic light scattering (DLS) graphs (size distribution by volume), showing the size distribution of the PE/PC SUV preparation, and appearance of additional peaks corresponding to vesicle clusters, 30 min after adding TEV protease and 3 μM MBP-2C (red solid line) or MBP-2C(ΔAH1) (orange dotted line) to SUVs (blue solid line). **(B)** Percentage of the total vesicle volume present in clusters (defined as particles with diameter > 100 nm), 30 min after adding TEV protease and 0.8 or 3 μM MBP-2C or MBP-2C(ΔAH1). Dots represent the average of triplicate measurements on the same SUV preparation, bars the average and error bars one standard deviation of the three independent replicates. Statistical significance by unpaired two-tailed Student's t-test; ns >0.05; **$p < 0.01$ **(C)** Computational slice through a representative cryo-electron tomogram of PE/PC SUVs, 30 min after adding TEV protease and 3 μM MBP-2C. Densities corresponding to 2C are pointed by red triangles. The right panel shows the corresponding three-dimensional segmentation showing 2C (red) and SUVs (yellow). Scale bar, 50 nm.

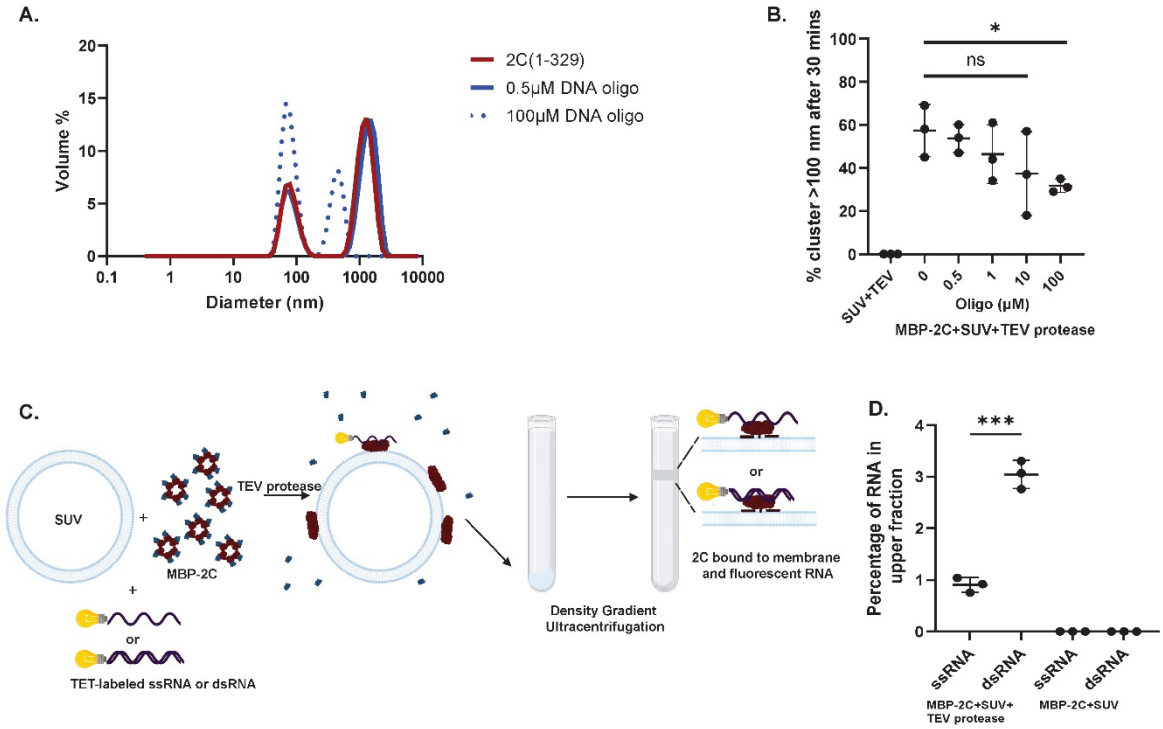

Figure 5: 2C preferentially recruits double-stranded RNA to membranes. (A) Representative DLS graphs (size distribution by volume), performed as for Fig. 4A with 3 μM 2C, but with the indicated concentrations of ssDNA oligonucleotide added. **(B)** Percentage of vesicle volume present as clusters (evaluated as for Fig. 4B), 30 min after addition of TEV protease, MBP-2C, and the indicated concentration of ssDNA oligonucleotide. Dots represent the average of triplicate measurements on the same SUV preparation, bars the average and error bars one standard deviation of the three independent replicates. Statistical significance by unpaired two-tailed Student's t test; ns >0.05; *$p < 0.05$. **(C)** Schematic representation of the flotation assay used to quantify RNA recruitment to membranes by 2C. The experiment is essentially performed as in Fig. 3A, except that MBP-2C is unlabeled, and the RNA (single-stranded, or annealed with a complementary strand for double-stranded) is labeled with TET fluorophore at its 5′ end (Fig. S8). Membrane-bound RNA is quantitated by measuring TET fluorescence in the upper fraction **(D)** Fluorescence from ssRNA and dsRNA in top fraction in the experiment outlined in (C). Dots represent the average of triplicate measurements on the same SUV preparation, bars the average and error bars one standard deviation of the three independent replicates. Statistical significance by unpaired two-tailed Student's t-test; ***$p < 0.001$.

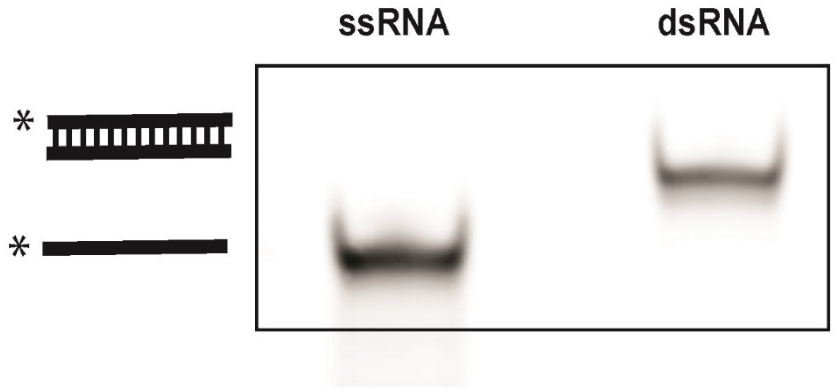

Figure S7: Characterization of fluorescent ssRNA and dsRNA. Fluorescence scan of non-denaturing polyacrylamide gel showing 5'TET-labelled ssRNA and 5'TET-labelled dsRNA.

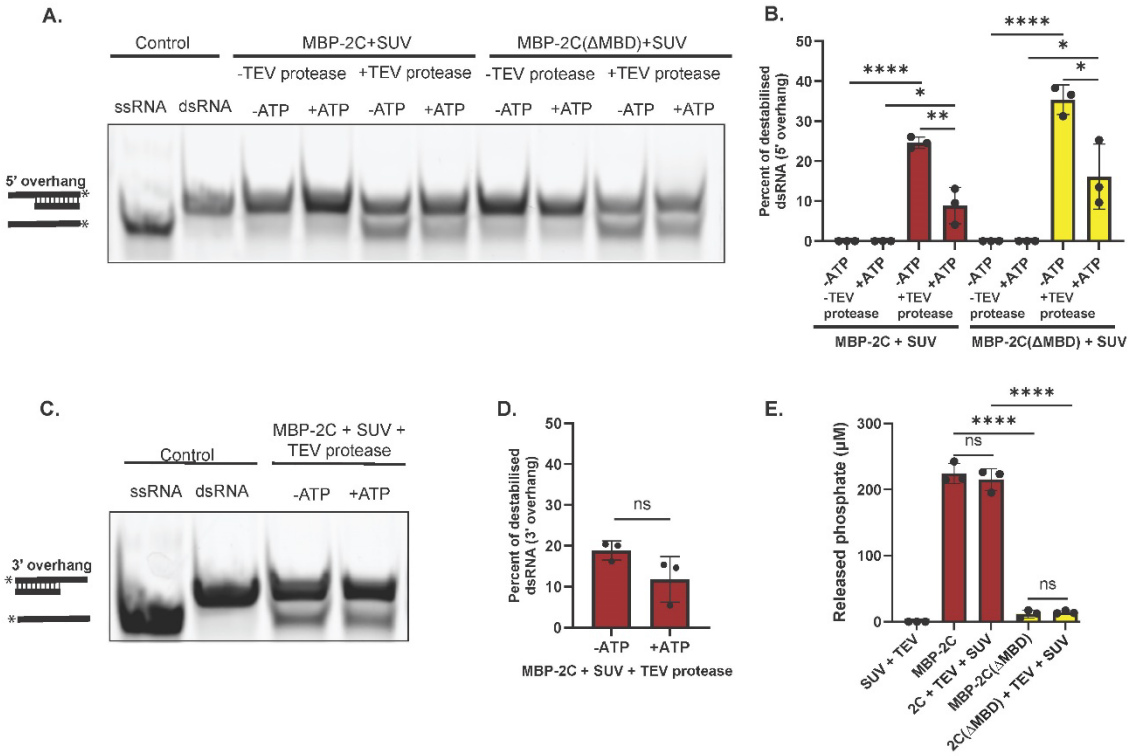

Figure 6: Membrane-bound, full-length 2C is an ATP-independent RNA chaperone. (A) Native polyacrylamide gel resolving dsRNA and ssRNA after a helicase assay. MBP-2C and MBP-2C(41-329) were incubated with dsRNA with a 5'overhang in the presence of SUVs, and presence or absence of TEV protease and Mg^{2+}-ATP. Lanes 1 and 2 from the left were loaded with ssRNA control and dsRNA substrate, respectively. The remaining lanes were loaded with RNA helicase reactions taken at the end of the two hour incubation, with proteins and reactants as indicated in the figure. A representative gel is shown, the experiment was performed in three independent replicates. **(B)** The percentage of total RNA signal (dsRNA and ssRNA) present as ssRNA is plotted for selected lanes of the gel in (A), and two independent replicates of the same experiment. Dots represent individual experiments, bars the average and error bars one standard deviation. The dsRNA lane was subtracted as background. Statistical significance by unpaired two-tailed Student's t-test; *$p < 0.05$; **$p < 0.01$; ****$p < 0.0001$. **(C)** Native polyacrylamide gel on a similar experiment to (A), but with a 3' overhang on the dsRNA. Lanes are labeled analogously to (A). **(D)** The percentage of total RNA signal (dsRNA and ssRNA) present as ssRNA is plotted for selected lanes of the gel in (C), and two independent replicates of the same experiment. Dots represent individual experiments, bars the average and error bars one standard deviation of the three independent replicates. The dsRNA lane was subtracted as background. Statistical significance by unpaired two-tailed Student's t test; ns > 0.05. **(E)** Colorimetric ATPase assay. MBP-2C and MBP-2C(41-329) were incubated with 0.4 mM ATP in the presence and absence of SUV+TEV protease. The amount of NTP hydrolyzed was determined and plotted. Dots represent individual experiments, bars the average and error bars one standard deviation. Statistical significance by unpaired two-tailed Student's t-test; ns > 0.05; ****$p < 0.0001$.

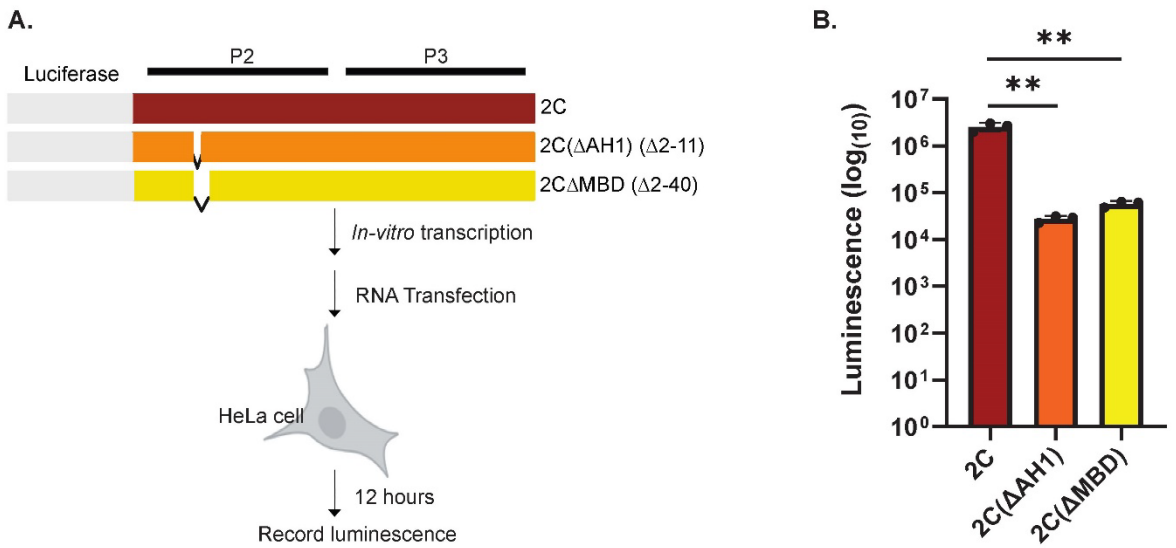

Figure 7: Truncation of AH1 or the MBD drastically reduces poliovirus replication. (A) Schematic representation of poliovirus replicons and their use. The replicons contained Renilla luciferase in place of the capsid region of the polyprotein, and the indicated deletions in the MBD of 2C. The first residue of 2C, glycine, was kept in both deletions since it is a core part of the protease cleavage site. In vitro-transcribed RNAs from these replicons were transfected into HeLa cells and luminescence was recorded 12 hours post-transfection. **(B)** Luminescence recorded for cells transfected with different poliovirus replicons. Dots represent individual experiments, bars the average, and error bars one standard deviation of the three independent replicates**.** Statistical significance by unpaired two-tailed Student's t-test; $^{**}p < 0.01$.

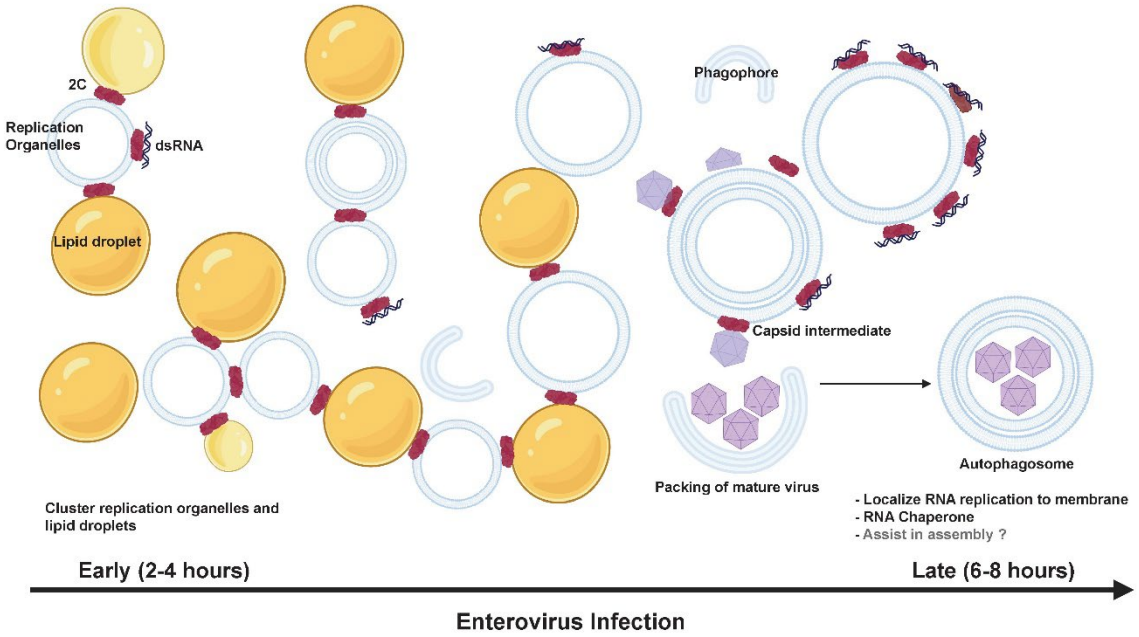

Figure 8: A model for the multiple roles of 2C in enterovirus replication. The model places the biochemical findings of this study into a suggested cellular context. At an early stage of infection, 2C serves to cluster replication organelle membranes and lipid droplets, while tethering the first viral dsRNA to the membrane. As the replication progresses, 2C is increasingly loaded with viral dsRNA and thus is a key component in localizing viral RNA replication to the replication organelle membranes. Our data suggest that 2C is an active ATPase but not and RNA helicase – a role which may be played by the polymerase 3D. Although not addressed in this study, the literature strongly suggests an additional role for 2C in capsid assembly and RNA loading, consistent with it being part of a "tethering complex" which tethers newly synthesized capsids to replication organelle membranes.

709 **Table 1: List of all the oligonucleotides used**

Oligo	Sequence 5'-3'	Type	Label
1	CCUCUAACCACAGUCUGAUC (20)	RNA	5' Tetrachlorofluorescein (TET)
2	GAUCAGACUGUGG UUAGAGG (20)	RNA	-
3	TGAATGCGGCTAATCCCAACCT (22)	DNA	-
4	AAAAAAAAAAAACCAGGCGACAUCAGCG (28)	RNA	3' Carboxyfluorescein (FAM)
5	CCAGGCGACAUCAGCGAAAAAAAAAAAA(28)	RNA	5' Carboxyfluorescein (FAM)
6	CGCUGAUGUCGCCUGG (16)	RNA	-

710

711

712

713 **Supplementary movie 1: Slices through cryo-electron tomogram showing vesicle clustering by 2C.** The
714 movie loops consecutive xy-planes of the cryo-electron tomogram shown in Fig. 4C.

715

716 **Supplementary movie 2. Surface model of cryo-electron tomogram showing vesicle clustering by 2C.** The
717 movie shows different views of the surface model of the tomogram shown in Fig. 4C.

718

References

1. Hyypia T, Hovi T, Knowles NJ, Stanway G. Classification of enteroviruses based on molecular and biological properties. J Gen Virol. 1997;78 (Pt 1):1-11. doi: 10.1099/0022-1317-78-1-1. PubMed PMID: 9010279.
2. Jiang P, Liu Y, Ma HC, Paul AV, Wimmer E. Picornavirus morphogenesis. Microbiol Mol Biol Rev. 2014;78(3):418-37. Epub 2014/09/04. doi: 10.1128/MMBR.00012-14. PubMed PMID: 25184560; PubMed Central PMCID: PMCPMC4187686.
3. Adams MJ, Lefkowitz EJ, King AM, Bamford DH, Breitbart M, Davison AJ, et al. Ratification vote on taxonomic proposals to the International Committee on Taxonomy of Viruses (2015). Arch Virol. 2015;160(7):1837-50. doi: 10.1007/s00705-015-2425-z. PubMed PMID: 25913692.
4. Murphy OC, Messacar K, Benson L, Bove R, Carpenter JL, Crawford T, et al. Acute flaccid myelitis: cause, diagnosis, and management. Lancet. 2021;397(10271):334-46. Epub 20201223. doi: 10.1016/S0140-6736(20)32723-9. PubMed PMID: 33357469; PubMed Central PMCID: PMCPMC7909727.
5. Holm-Hansen CC, Midgley SE, Fischer TK. Global emergence of enterovirus D68: a systematic review. Lancet Infect Dis. 2016;16(5):e64-e75. Epub 20160224. doi: 10.1016/S1473-3099(15)00543-5. PubMed PMID: 26929196.
6. Lukashev AN, Lashkevich VA, Ivanova OE, Koroleva GA, Hinkkanen AE, Ilonen J. Recombination in circulating enteroviruses. J Virol. 2003;77(19):10423-31. doi: 10.1128/jvi.77.19.10423-10431.2003. PubMed PMID: 12970427; PubMed Central PMCID: PMCPMC228507.
7. Chevaliez S, Szendroi A, Caro V, Balanant J, Guillot S, Berencsi G, et al. Molecular comparison of echovirus 11 strains circulating in Europe during an epidemic of multisystem hemorrhagic disease of infants indicates that evolution generally occurs by recombination. Virology. 2004;325(1):56-70. doi: 10.1016/j.virol.2004.04.026. PubMed PMID: 15231386.
8. Lukashev AN. Role of recombination in evolution of enteroviruses. Rev Med Virol. 2005;15(3):157-67. doi: 10.1002/rmv.457. PubMed PMID: 15578739.
9. Martini M, Orsini D. The fight against poliomyelitis through the history: past, present and hopes for the future. Albert Sabin's missing Nobel and his "gift to all the world's children". Vaccine. 2022;40(47):6802-5. Epub 20221014. doi: 10.1016/j.vaccine.2022.09.088. PubMed PMID: 36244880.
10. Thompson KM, Lauring AS, Pollard AJ, Andino R, Bandyopadhyay AS, Berkley S, et al. Polio eradication: Addressing the hurdles on the last mile. Cell. 2023;186(1):1-4. doi: 10.1016/j.cell.2022.12.021. PubMed PMID: 36608647.
11. Pons-Salort M, Parker EP, Grassly NC. The epidemiology of non-polio enteroviruses: recent advances and outstanding questions. Curr Opin Infect Dis. 2015;28(5):479-87. doi: 10.1097/QCO.0000000000000187. PubMed PMID: 26203854; PubMed Central PMCID: PMCPMC6624138.
12. Chapman NM, Kim KS. Persistent coxsackievirus infection: enterovirus persistence in chronic myocarditis and dilated cardiomyopathy. Curr Top Microbiol Immunol. 2008;323:275-92. doi: 10.1007/978-3-540-75546-3_13. PubMed PMID: 18357775.
13. Anasir MI, Zarif F, Poh CL. Antivirals blocking entry of enteroviruses and therapeutic potential. J Biomed Sci. 2021;28(1):10. Epub 20210115. doi: 10.1186/s12929-021-00708-8. PubMed PMID: 33451326; PubMed Central PMCID: PMCPMC7811253.
14. Sun J, Yogarajah T, Lee RCH, Kaur P, Inoue M, Tan YW, et al. Drug repurposing of pyrimidine analogs as potent antiviral compounds against human enterovirus A71 infection with potential clinical applications. Sci Rep. 2020;10(1):8159. Epub 20200518. doi: 10.1038/s41598-020-65152-4. PubMed PMID: 32424333; PubMed Central PMCID: PMCPMC7235037.
15. Kejriwal R, Evans T, Calabrese J, Swistak L, Alexandrescu L, Cohen M, et al. Development of Enterovirus Antiviral Agents That Target the Viral 2C Protein. ChemMedChem. 2023;18(10):e202200541. Epub 20230310. doi: 10.1002/cmdc.202200541. PubMed PMID: 36792530.
16. Caliguiri LA, Tamm I. Membranous structures associated with translation and transcription of poliovirus RNA. Science. 1969;166(3907):885-6. doi: 10.1126/science.166.3907.885. PubMed PMID: 4310189.

17. Bienz K, Egger D, Rasser Y, Bossart W. Kinetics and location of poliovirus macromolecular synthesis in correlation to virus-induced cytopathology. Virology. 1980;100(2):390-9. doi: 10.1016/0042-6822(80)90530-9. PubMed PMID: 6243433.
18. Bienz K, Egger D, Rasser Y, Bossart W. Intracellular distribution of poliovirus proteins and the induction of virus-specific cytoplasmic structures. Virology. 1983;131(1):39-48. doi: 10.1016/0042-6822(83)90531-7. PubMed PMID: 6316654.
19. Dahmane S, Kerviel A, Morado DR, Shankar K, Ahlman B, Lazarou M, et al. Membrane-assisted assembly and selective secretory autophagy of enteroviruses. Nature communications. 2022;13(1):5986. Epub 2022/10/11. doi: 10.1038/s41467-022-33483-7. PubMed PMID: 36216808; PubMed Central PMCID: PMCPMC9550805.
20. Limpens RW, van der Schaar HM, Kumar D, Koster AJ, Snijder EJ, van Kuppeveld FJ, et al. The transformation of enterovirus replication structures: a three-dimensional study of single- and double-membrane compartments. mBio. 2011;2(5). Epub 2011/10/06. doi: 10.1128/mBio.00166-11. PubMed PMID: 21972238; PubMed Central PMCID: PMCPMC3187575.
21. Strating JR, van der Linden L, Albulescu L, Bigay J, Arita M, Delang L, et al. Itraconazole inhibits enterovirus replication by targeting the oxysterol-binding protein. Cell Rep. 2015;10(4):600-15. Epub 20150129. doi: 10.1016/j.celrep.2014.12.054. PubMed PMID: 25640182; PubMed Central PMCID: PMCPMC4383725.
22. Ilnytska O, Santiana M, Hsu NY, Du WL, Chen YH, Viktorova EG, et al. Enteroviruses harness the cellular endocytic machinery to remodel the host cell cholesterol landscape for effective viral replication. Cell Host Microbe. 2013;14(3):281-93. doi: 10.1016/j.chom.2013.08.002. PubMed PMID: 24034614; PubMed Central PMCID: PMCPMC3802520.
23. Laufman O, Perrino J, Andino R. Viral Generated Inter-Organelle Contacts Redirect Lipid Flux for Genome Replication. Cell. 2019;178(2):275-89 e16. Epub 2019/06/18. doi: 10.1016/j.cell.2019.05.030. PubMed PMID: 31204099; PubMed Central PMCID: PMCPMC7077330.
24. Schlegel A, Giddings TH, Jr., Ladinsky MS, Kirkegaard K. Cellular origin and ultrastructure of membranes induced during poliovirus infection. J Virol. 1996;70(10):6576-88. doi: 10.1128/JVI.70.10.6576-6588.1996. PubMed PMID: 8794292; PubMed Central PMCID: PMCPMC190698.
25. Hsu NY, Ilnytska O, Belov G, Santiana M, Chen YH, Takvorian PM, et al. Viral reorganization of the secretory pathway generates distinct organelles for RNA replication. Cell. 2010;141(5):799-811. Epub 2010/06/01. doi: S0092-8674(10)00369-7 [pii]

10.1016/j.cell.2010.03.050. PubMed PMID: 20510927; PubMed Central PMCID: PMC2982146.
26. Miller S, Krijnse-Locker J. Modification of intracellular membrane structures for virus replication. Nature reviews. 2008;6(5):363-74. Epub 2008/04/17. doi: nrmicro1890 [pii]

10.1038/nrmicro1890. PubMed PMID: 18414501.
27. Melia CE, van der Schaar HM, de Jong AWM, Lyoo HR, Snijder EJ, Koster AJ, et al. The Origin, Dynamic Morphology, and PI4P-Independent Formation of Encephalomyocarditis Virus Replication Organelles. mBio. 2018;9(2). Epub 20180417. doi: 10.1128/mBio.00420-18. PubMed PMID: 29666283; PubMed Central PMCID: PMCPMC5904412.
28. Bienz K, Egger D, Pfister T, Troxler M. Structural and functional characterization of the poliovirus replication complex. J Virol. 1992;66(5):2740-7. doi: 10.1128/JVI.66.5.2740-2747.1992. PubMed PMID: 1313898; PubMed Central PMCID: PMCPMC241029.
29. Takeda N, Kuhn RJ, Yang CF, Takegami T, Wimmer E. Initiation of poliovirus plus-strand RNA synthesis in a membrane complex of infected HeLa cells. J Virol. 1986;60(1):43-53. doi: 10.1128/JVI.60.1.43-53.1986. PubMed PMID: 3018300; PubMed Central PMCID: PMCPMC253900.
30. Guo H, Li Y, Liu G, Jiang Y, Shen S, Bi R, et al. A second open reading frame in human enterovirus determines viral replication in intestinal epithelial cells. Nat Commun. 2019;10(1):4066. Epub 20190906. doi: 10.1038/s41467-019-12040-9. PubMed PMID: 31492846; PubMed Central PMCID: PMCPMC6731315.
31. Gorbalenya AE, Koonin EV, Wolf YI. A new superfamily of putative NTP-binding domains encoded by genomes of small DNA and RNA viruses. FEBS Lett. 1990;262(1):145-8. doi: 10.1016/0014-5793(90)80175-i. PubMed PMID: 2156730.

32. Pfister T, Wimmer E. Characterization of the nucleoside triphosphatase activity of poliovirus protein 2C reveals a mechanism by which guanidine inhibits poliovirus replication. J Biol Chem. 1999;274(11):6992-7001. doi: 10.1074/jbc.274.11.6992. PubMed PMID: 10066753.
33. Teterina NL, Kean KM, Gorbalenya AE, Agol VI, Girard M. Analysis of the functional significance of amino acid residues in the putative NTP-binding pattern of the poliovirus 2C protein. J Gen Virol. 1992;73 (Pt 8):1977-86. doi: 10.1099/0022-1317-73-8-1977. PubMed PMID: 1322957.
34. Liu Y, Wang C, Mueller S, Paul AV, Wimmer E, Jiang P. Direct interaction between two viral proteins, the nonstructural protein 2C and the capsid protein VP3, is required for enterovirus morphogenesis. PLoS Pathog. 2010;6(8):e1001066. Epub 20100826. doi: 10.1371/journal.ppat.1001066. PubMed PMID: 20865167; PubMed Central PMCID: PMCPMC2928791.
35. Vance LM, Moscufo N, Chow M, Heinz BA. Poliovirus 2C region functions during encapsidation of viral RNA. J Virol. 1997;71(11):8759-65. Epub 1997/10/29. PubMed PMID: 9343235; PubMed Central PMCID: PMCPMC192341.
36. Li JP, Baltimore D. Isolation of poliovirus 2C mutants defective in viral RNA synthesis. J Virol. 1988;62(11):4016-21. doi: 10.1128/JVI.62.11.4016-4021.1988. PubMed PMID: 2845120; PubMed Central PMCID: PMCPMC253830.
37. Pincus SE, Diamond DC, Emini EA, Wimmer E. Guanidine-selected mutants of poliovirus: mapping of point mutations to polypeptide 2C. J Virol. 1986;57(2):638-46. doi: 10.1128/JVI.57.2.638-646.1986. PubMed PMID: 3003395; PubMed Central PMCID: PMCPMC252779.
38. Tolskaya EA, Romanova LI, Kolesnikova MS, Gmyl AP, Gorbalenya AE, Agol VI. Genetic studies on the poliovirus 2C protein, an NTPase. A plausible mechanism of guanidine effect on the 2C function and evidence for the importance of 2C oligomerization. J Mol Biol. 1994;236(5):1310-23. doi: 10.1016/0022-2836(94)90060-4. PubMed PMID: 8126722.
39. Guan H, Tian J, Zhang C, Qin B, Cui S. Crystal structure of a soluble fragment of poliovirus 2CATPase. PLoS Pathog. 2018;14(9):e1007304. Epub 20180919. doi: 10.1371/journal.ppat.1007304. PubMed PMID: 30231078; PubMed Central PMCID: PMCPMC6166989.
40. Guan H, Tian J, Qin B, Wojdyla JA, Wang B, Zhao Z, et al. Crystal structure of 2C helicase from enterovirus 71. Sci Adv. 2017;3(4):e1602573. Epub 2017/05/17. doi: 10.1126/sciadv.1602573. PubMed PMID: 28508043; PubMed Central PMCID: PMCPMC5409451.
41. Hurdiss DL, El Kazzi P, Bauer L, Papageorgiou N, Ferron FP, Donselaar T, et al. Fluoxetine targets an allosteric site in the enterovirus 2C AAA+ ATPase and stabilizes a ring-shaped hexameric complex. Sci Adv. 2022;8(1):eabj7615. Epub 20220105. doi: 10.1126/sciadv.abj7615. PubMed PMID: 34985963; PubMed Central PMCID: PMCPMC8730599.
42. Pfister T, Jones KW, Wimmer E. A cysteine-rich motif in poliovirus protein 2C(ATPase) is involved in RNA replication and binds zinc in vitro. J Virol. 2000;74(1):334-43. doi: 10.1128/jvi.74.1.334-343.2000. PubMed PMID: 10590122; PubMed Central PMCID: PMCPMC111544.
43. Adams P, Kandiah E, Effantin G, Steven AC, Ehrenfeld E. Poliovirus 2C protein forms homo-oligomeric structures required for ATPase activity. J Biol Chem. 2009;284(33):22012-21. Epub 20090611. doi: 10.1074/jbc.M109.031807. PubMed PMID: 19520852; PubMed Central PMCID: PMCPMC2755925.
44. Yeager C, Carter G, Gohara DW, Yennawar NH, Enemark EJ, Arnold JJ, et al. Enteroviral 2C protein is an RNA-stimulated ATPase and uses a two-step mechanism for binding to RNA and ATP. Nucleic Acids Res. 2022;50(20):11775-98. Epub 2022/11/19. doi: 10.1093/nar/gkac1054. PubMed PMID: 36399514; PubMed Central PMCID: PMCPMC9723501.
45. Xia H, Wang P, Wang GC, Yang J, Sun X, Wu W, et al. Human Enterovirus Nonstructural Protein 2CATPase Functions as Both an RNA Helicase and ATP-Independent RNA Chaperone. PLoS Pathog. 2015;11(7):e1005067. Epub 20150728. doi: 10.1371/journal.ppat.1005067. PubMed PMID: 26218680; PubMed Central PMCID: PMCPMC4517893.
46. Paul AV, Molla A, Wimmer E. Studies of a putative amphipathic helix in the N-terminus of poliovirus protein 2C. Virology. 1994;199(1):188-99. doi: 10.1006/viro.1994.1111. PubMed PMID: 8116242.

880 47. Echeverri AC, Dasgupta A. Amino terminal regions of poliovirus 2C protein mediate
881 membrane binding. Virology. 1995;208(2):540-53. doi: 10.1006/viro.1995.1185. PubMed PMID:
882 7747426.
883 48. Echeverri A, Banerjee R, Dasgupta A. Amino-terminal region of poliovirus 2C protein is
884 sufficient for membrane binding. Virus Res. 1998;54(2):217-23. doi: 10.1016/s0168-1702(98)00016-1.
885 PubMed PMID: 9696129.
886 49. Jumper J, Evans R, Pritzel A, Green T, Figurnov M, Ronneberger O, et al. Highly
887 accurate protein structure prediction with AlphaFold. Nature. 2021;596(7873):583-9. Epub 20210715.
888 doi: 10.1038/s41586-021-03819-2. PubMed PMID: 34265844; PubMed Central PMCID:
889 PMCPMC8371605.
890 50. Goddard TD, Huang CC, Meng EC, Pettersen EF, Couch GS, Morris JH, et al. UCSF
891 ChimeraX: Meeting modern challenges in visualization and analysis. Protein Sci. 2018;27(1):14-25.
892 Epub 2017/07/16. doi: 10.1002/pro.3235. PubMed PMID: 28710774; PubMed Central PMCID:
893 PMCPMC5734306.
894 51. Papageorgiou N, Coutard B, Lantez V, Gautron E, Chauvet O, Baronti C, et al. The 2C
895 putative helicase of echovirus 30 adopts a hexameric ring-shaped structure. Acta Crystallogr D Biol
896 Crystallogr. 2010;66(Pt 10):1116-20. Epub 20100918. doi: 10.1107/S090744491002809X. PubMed
897 PMID: 20944244.
898 52. Wolff G, Melia CE, Snijder EJ, Barcena M. Double-Membrane Vesicles as Platforms for
899 Viral Replication. Trends Microbiol. 2020;28(12):1022-33. Epub 2020/06/17. doi:
900 10.1016/j.tim.2020.05.009. PubMed PMID: 32536523; PubMed Central PMCID: PMCPMC7289118.
901 53. Wang C, Jiang P, Sand C, Paul AV, Wimmer E. Alanine scanning of poliovirus
902 2CATPase reveals new genetic evidence that capsid protein/2CATPase interactions are essential for
903 morphogenesis. J Virol. 2012;86(18):9964-75. Epub 20120703. doi: 10.1128/JVI.00914-12. PubMed
904 PMID: 22761387; PubMed Central PMCID: PMCPMC3446611.
905 54. Rodriguez PL, Carrasco L. Poliovirus protein 2C contains two regions involved in RNA
906 binding activity. J Biol Chem. 1995;270(17):10105-12. doi: 10.1074/jbc.270.17.10105. PubMed PMID:
907 7730315.
908 55. Rodriguez PL, Carrasco L. Poliovirus protein 2C has ATPase and GTPase activities. J
909 Biol Chem. 1993;268(11):8105-10. PubMed PMID: 8385138.
910 56. Mirzayan C, Wimmer E. Genetic analysis of an NTP-binding motif in poliovirus
911 polypeptide 2C. Virology. 1992;189(2):547-55. doi: 10.1016/0042-6822(92)90578-d. PubMed PMID:
912 1322588.
913 57. Cohen L, Kean KM, Girard M, Van der Werf S. Effects of P2 cleavage site mutations on
914 poliovirus polyprotein processing. Virology. 1996;224(1):34-42. Epub 1996/10/01. doi:
915 10.1006/viro.1996.0504. PubMed PMID: 8862397.
916 58. Dahmane S, Shankar K, Carlson LA. A 3D view of how enteroviruses hijack autophagy.
917 Autophagy. 2022:1-3. Epub 2022/12/07. doi: 10.1080/15548627.2022.2153572. PubMed PMID:
918 36471479.
919 59. Dubankova A, Humpolickova J, Klima M, Boura E. Negative charge and membrane-
920 tethered viral 3B cooperate to recruit viral RNA dependent RNA polymerase 3D (pol). Scientific reports.
921 2017;7(1):17309. Epub 2017/12/13. doi: 10.1038/s41598-017-17621-6. PubMed PMID: 29230036;
922 PubMed Central PMCID: PMCPMC5725453.
923 60. Cho MW, Richards OC, Dmitrieva TM, Agol V, Ehrenfeld E. RNA duplex unwinding
924 activity of poliovirus RNA-dependent RNA polymerase 3Dpol. J Virol. 1993;67(6):3010-8. Epub
925 1993/06/01. doi: 10.1128/JVI.67.6.3010-3018.1993. PubMed PMID: 8388485; PubMed Central
926 PMCID: PMCPMC237637.
927 61. Baggen J, Thibaut HJ, Strating J, van Kuppeveld FJM. The life cycle of non-polio
928 enteroviruses and how to target it. Nature reviews. 2018;16(6):368-81. Epub 2018/04/08. doi:
929 10.1038/s41579-018-0005-4. PubMed PMID: 29626210.
930 62. Young G, Hundt N, Cole D, Fineberg A, Andrecka J, Tyler A, et al. Quantitative mass
931 imaging of single biological macromolecules. Science. 2018;360(6387):423-7. doi:
932 10.1126/science.aar5839. PubMed PMID: 29700264; PubMed Central PMCID: PMCPMC6103225.
933 63. Sievers F, Wilm A, Dineen D, Gibson TJ, Karplus K, Li W, et al. Fast, scalable generation
934 of high-quality protein multiple sequence alignments using Clustal Omega. Mol Syst Biol. 2011;7:539.

935 Epub 20111011. doi: 10.1038/msb.2011.75. PubMed PMID: 21988835; PubMed Central PMCID:
936 PMCPMC3261699.
937 64. Gautier R, Douguet D, Antonny B, Drin G. HELIQUEST: a web server to screen
938 sequences with specific alpha-helical properties. Bioinformatics. 2008;24(18):2101-2. Epub 20080728.
939 doi: 10.1093/bioinformatics/btn392. PubMed PMID: 18662927.
940 65. Mastronarde DN, Held SR. Automated tilt series alignment and tomographic
941 reconstruction in IMOD. J Struct Biol. 2017;197(2):102-13. Epub 20160719. doi:
942 10.1016/j.jsb.2016.07.011. PubMed PMID: 27444392; PubMed Central PMCID: PMCPMC5247408.
943 66. Zheng SQ, Palovcak E, Armache JP, Verba KA, Cheng Y, Agard DA. MotionCor2:
944 anisotropic correction of beam-induced motion for improved cryo-electron microscopy. Nat Methods.
945 2017;14(4):331-2. Epub 2017/03/03. doi: 10.1038/nmeth.4193. PubMed PMID: 28250466; PubMed
946 Central PMCID: PMCPMC5494038.
947 67. Rohou A, Grigorieff N. CTFFIND4: Fast and accurate defocus estimation from electron
948 micrographs. J Struct Biol. 2015;192(2):216-21. Epub 2015/08/19. doi: 10.1016/j.jsb.2015.08.008.
949 PubMed PMID: 26278980; PubMed Central PMCID: PMCPMC6760662.
950 68. Liu YT, Zhang H, Wang H, Tao CL, Bi GQ, Zhou ZH. Isotropic reconstruction for
951 electron tomography with deep learning. Nat Commun. 2022;13(1):6482. Epub 20221029. doi:
952 10.1038/s41467-022-33957-8. PubMed PMID: 36309499; PubMed Central PMCID:
953 PMCPMC9617606.

954